ACS APPLIED MATERIALS & INTERFACES

www.acsami.org

Research Article

Tuning Mixed Conduction between Ionic and Electronic Transport in Blended OMIECs via Phase Separation and Selective Dissolution

Qizhe Tang, Isabelle Barwick, Qi Han, Benjamin Watts, Lars Thomsen, Julian Hungenberg, Matthew Gebert, Fabian Eller, Eva M. Herzig, Mukundan Thelakkat, Keying Guo, and Christopher R. McNeill*

Cite This: *ACS Appl. Mater. Interfaces* 2026, 18, 30250−30268

Read Online

ACCESS | Metrics & More | Article Recommendations | Supporting Information

ABSTRACT: This study reveals how the morphology of organic mixed ionic-electronic conductors (OMIECs) controls the mixed ionic-electronic transport of organic electrochemical transistors (OECTs). Two p-type OMIECs with oligo-ethylene glycol (OEG) side chains, namely P3MEEET and P3MEEMT, are blended with polystyrene (PS) to produce laterally phase-separated morphologies. By varying the ratio between OMIEC and PS, distinct morphologies are created via nucleation and growth and via spinodal decomposition. Furthermore, porous films are fabricated through the selective dissolution of PS, providing a direct comparison between blend and porous structures on OECT performance. In blends, the reduced ion injection area significantly enhances the mobility (μ) and figure of merit (μC^*). Due to the hydrophilic nature of the OMIECs, adding pores to the films does not have a positive effect on signal amplification but improves ion storage via side injection and increases the effective volumetric capacitance (C^*). Comparing the two OMIECs studied, porous samples based on P3MEEMT experience a greater benefit from electrolyte side injection. Both blend and porous samples are characterized using a range of techniques, including spectroelectrochemistry (SEC), atomic force microscopy (AFM), scanning transmission X-ray microscopy (STXM), quartz crystal microbalance (QCM), along with ex situ and in situ grazing-incidence wide-angle X-ray scattering (GIWAXS) to unravel the mechanism of the mixed ionic-electronic transport from both an ionic and electronic perspective.

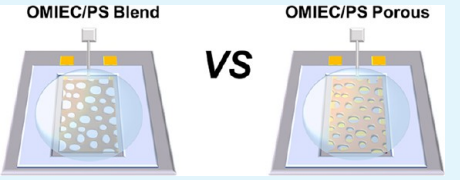

KEYWORDS: *OECTs, morphology, selective dissolution, organic electronics, electrochemistry, polymer characterization, phase separation*

INTRODUCTION

Organic mixed ionic-electronic conductors (OMIECs) are attractive materials for biocompatible devices due to their superior sensing capabilities and design flexibility. These properties make OMIECs suitable for diverse environments,[1−9] with OMIECs showing promise for practical implementation in real-life contexts such as stretchable electronics,[10−12] wearable devices,[13] neuromorphic systems,[14,15] clinical diagnosis,[4,16−19] and drug delivery.[20,21] All of these applications are based on organic electrochemical transistors (OECTs), which can convert and amplify biological signals in the form of ions in an electrolyte into an electronic current under low driving voltages.[1,5,8,22,23] OECTs work by applying a gate bias that induces electronic charge carriers in the polymer channel, accompanied by the penetration of counterions from the electrolyte to maintain charge neutrality within the bulk of the OMIEC film, assisted by its hydrophilic nature,[22,23] thereby generating charge carriers within the bulk of the polymer film of OMIEC materials.[6,24] This bulk electrochemical doping of the film then enables a drain current to flow between two source/drain electrodes, establishing a mixed ionic-electronic system.[6,22] The ionic conduction process plays a critical role in the operation of OECTs.[25] Unlike traditional field-effect transistors that can only induce charge carriers close to the dielectric/semiconductor interface, the ion penetration throughout the bulk of the OECTs substantially increases the amount of charge carriers induced within the channel, resulting in a significant boost of current with a low-voltage requirement.[22,26] However, elevated uptake of water negatively affects the electronic conductivity as a result of the swelling of the polymer film, making the ionic transport process a double-edged sword for the overall performance of OECTs.[6,27,28] Thus, it is essential to achieve a balance between swelling and ionic transport on the one hand and electronic transport on the other hand to optimize device performance.[23,29,30]

The structural and morphological properties of OMIEC materials strongly affect the performance of OECTs, with recent work focusing on understanding the effect of polymer chemistry,[31−41] thin-film crystallinity,[42−45] and device geo-

Received: March 20, 2026
Revised: May 8, 2026
Accepted: May 8, 2026
Published: May 20, 2026

metries[10,42,46−51] on the mechanism of mixed ionic-electronic transport. The swelling process, in particular, is highly dependent on the polymer chemistry. A recent study illustrated the swelling mechanism of poly(3-([2-(2-methoxyethoxy)-ethoxy]methyl)thiophene-2,5-diyl) (P3MEEMT) in the hydrated and doped states. In the hydrated, neutral state, expansion of the crystalline lattice was observed because of the hydrophilic nature of the ethylene glycol side chains. During the process of doping and dedoping, water is seen to be absorbed and repelled more so in the amorphous regions compared to the crystalline regions.[43] Notably, these swelling and deswelling processes are reversible. Similarly, in the case of poly[2,5-bis(thiophenyl)-1,4-bis(2-(2-(2-methoxyethoxy)-ethoxy)ethoxy)benzene] (PB2T-TEG), ions can be intercalated or extracted within polymer chains at the crystalline domains, leading to a reversible phase transition through lattice expansion.[52] The side-chain-free polymer poly(benzimidazobenzophenanthroline) (BBL), however, exhibits an irreversible swelling process: during deswelling, water molecules are not able to be fully removed between the gap of rigid backbones.[32] Coupled with the swelling effect, the ionic transport process primarily involves the drift of ions within the amorphous domains. Although ethylene glycol side chains facilitate the migration of water molecules and ions, they largely avoid the crystalline domains that represent barriers to ion transport in the swollen state, lengthening the effective drift pathway of ions compared to purely amorphous regions.[42] The impact of crystallization shows a complex scenario regarding its potential to either enhance or restrict electronic transport in OECTs combined with swelling and ionic transport. The increased crystallization caused by thermal annealing negatively affects electronic transport in the specific p-type polymer P3MEEMT by blocking the motion of charge carriers due to the formation of heterogeneity inside the bulk between amorphous and crystallized regions.[43] In contrast, a recent study of NDI-based n-type materials suggested that enhanced crystallization through thermal annealing significantly boosts electronic mobility by establishing rigid networks between crystallized regions.[44]

The geometry of the device is an essential factor in the performance of the OECTs. Vertical OECTs (v-OECTs), as a popular configuration, have been widely utilized in high-density integrated circuits.[15,46,47,53−55] In terms of mixed ionic-electronic transport, a key lesson learned from v-OECTs is that lateral ion injection (as opposed to vertical injection in conventional OECTs) can be beneficial for device performance, especially for specific polymer film textures.[42,47] One way to facilitate side injection from an ionic perspective is by fabricating laterally patterned (e.g., striped) films through lithography, which can produce precisely patterned films that allow for ion injection from both top and side directions. A recent study found that increasing the area of lateral injection significantly enhances the performance of poly(3-hexylthiophene) (P3HT)-based devices.[48] This study also elucidated that films with mixed crystallite orientations experience the greatest benefit from side injection.[48] Another approach for promoting side injection in OECTs involves the formation of pores within the film.[10,49] The breath-figure technique has been widely used to create porous polymer films; by spin-coating in a humid environment, pores are formed via the condensation of water droplets during solvent evaporation.[56] This method has been employed to significantly enhance the transconductance of OECTs based on OMIECs with alkyl side chains and oligoethylene glycol (OEG) side chains.[51] Together, these approaches to introduce side injection in OECTs highlight the critical role of film geometry in facilitating the injection and transport of ions for optimizing the device performance.

While the introduction of side injection of ions focuses on enhancing ionic transport for the performance of OECTs, it is equally important to consider electronic transport. Blending active polymers with insulating polymers is regarded as an effective way to improve the electronic mobility of the devices.[57−59] In hydrophilic polymers, the incorporation of insulating polymers could reduce excessive swelling, which is a primary factor contributing to the decreased electronic transport in OECTs. A good example of this is the blending of p(N-T) with polystyrene (PS) (10 kDa) at a ratio of 1:6. Upon blending, the product of the electronic mobility and volumetric capacitance (μC^*), also known as the figure of merit, was shown to exhibit a 3-fold enhancement to pristine p(N-T), with the reduced swelling contributing to the stabilization of the motion of charge carriers.[60] Another good example is the blending of poly(3-(methoxyethoxyethoxy)-thiophene) (P3MEET) with the radical polymers poly(4-ethylenedioxythiophene-*co*-ethylene oxide) (PTEO) and poly(4-episulfide-2,2,6,6-tetramethylpiperidine-1-oxyl) (PTES), demonstrating a significant boost of electronic mobility and μC^*. The addition of radical polymers also provided a 3 to 4-fold improvement in volumetric capacitance, while also reducing the threshold voltage.[61] However, the blending of two polymers does not always produce a uniform film, alternatively, phase separation may occur.[62,63] Phase-separated blends of P3HT and PS were investigated in a study focused on ion-gel gated OECTs, where the phase-separated blend exhibited a pronounced enhancement of electronic mobility with respect to the neat P3HT film.[64] Another study studied the blending of P3HT and poly(1,4-butylene adipate) (PBA) that resulted in vertical phase separation with PBA enriched at the film surface. By dissolving the PBA, a rough surface on the film could be realized thereby optimizing the contact area between P3HT and ion-gel electrolyte, enhancing both ionic and electronic mobility.[50] In terms of phase-separated blends of semiconducting and insulating polymers, despite some studies focusing on alkyl-based hydrophobic OECTs with ion-gel gated electrolytes, there have been few studies of the effect of blending hydrophilic OMIECs in liquid electrolyte gated OECTs.

Motivated by the above investigations on the effect of swelling on mixed ionic-electronic transport and the enhancements achieved through lateral injection and blending with insulating polymers, we report the first comparative analysis of mixed ionic-electronic transport in phase-separated and porous morphologies. Laterally phase-separated morphologies are produced by blending of P3MEEET and P3MEEMT with PS, with phase separation produced via nucleation and growth or spinodal decomposition, depending on the blend ratio. Porous films are then realized through the selective dissolution of PS using cyclohexane. Atomic force microscopy (AFM) and scanning transmission X-ray spectromicroscopy (STXM) are employed to investigate the lateral phase separation and chemical composition of blended and porous samples, effectively demonstrating well phase-separated blends and high-purity porous films. During doping, notable changes in the polaron peaks are observed in the porous samples of P3MEEMT series when compared with the blends, while the

https://doi.org/10.1021/acsami.6c05714
ACS Appl. Mater. Interfaces 2026, 18, 30250−30268

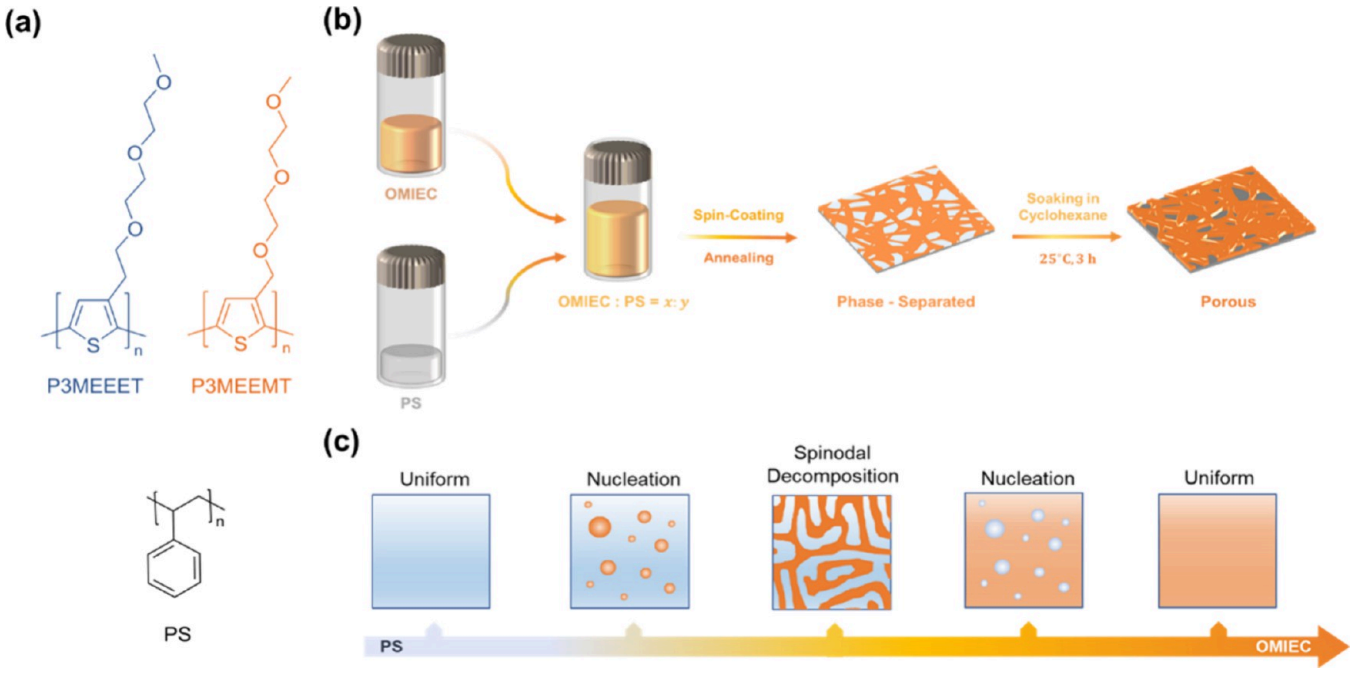

Figure 1. (a) Chemical structures of P3MEEMT, P3MEEET, and PS. (b) Illustration of blending-induced phase separation and selective dissolution. (c) Distinct phase-separation mechanisms via nucleation and spinodal decomposition by adjusting the ratio between OMIEC and PS.

P3MEEET series exhibits consistency between the porous and blend samples, indicating that P3MEEMT benefits more than P3MEEET in terms of lateral ion injection. From the perspective of device performance, the blends demonstrate significant improvements in electronic transport and figure of merit (μC^*) in both the P3MEEET and P3MEEMT series, whereas porous structures adversely affect electronic transport. Conversely, the porous structure demonstrates a notable enhancement in ionic transport by improving the effective volumetric capacitance (C^*) and reducing the response time. The quartz crystal microbalance (QCM) technique is employed to examine the swelling effect in blend and porous samples in relation to pure samples, while both ex-situ and in situ electrochemical doping grazing incidence wide-angle X-ray scattering (GIWAXS) are conducted to explore the impact of passive and active swelling on the crystalline domains within the blends and porous systems. From the perspective of these combined characterizations, we elucidate the mechanism underlying the mixed ionic-electronic transport in the blended and porous systems of P3MEEET and P3MEEMT, thereby enhancing our understanding of the influence of blends and pores from both ionic and electronic perspectives.

RESULTS AND DISCUSSION

Fabrication of Phase-Separated Blend and Porous Films

P3MEEMT and P3MEEET were selected as the active polymers (Figure 1a), with PS selected as the insulating polymer for blending. The major difference between P3MEEMT and P3MEEET is the presence of an ethyl spacer between the thiophene backbone and the glycol side chain in P3MEEET instead of a methyl spacer in the case of P3MEEMT. This small difference in their chemical structure leads to a pronounced difference in their passive and active swelling behavior: P3MEEMT exhibits greater passive swelling compared to P3MEEET, whereas P3MEEET exhibits enhanced active swelling in the doping stage.[31] These differences make for an interesting study of the effects of blending and porous structure on the behavior and OECT performance of P3MEEMT and P3MEEET.

To fabricate various blend and porous structured films, we first blended the OMIECs (P3MEEET or P3MEEMT) and PS (10 g/L in chloroform) at different blending ratios (v/v) (see Figure 1b). Figure 2a–f shows the AFM results that reveal the different phase-separated morphologies produced for the P3MEEET:PS films for the different ratios (see Figure S1 for P3MEEMT:PS blends). Examining the morphologies produced as a function of the blend ratio, lateral phase separation is observed over the range of OMIEC:PS from 4:12 (v/v) to 12:4 (v/v). Since the relative area of the dark phases (lower height) increases as the percentage of P3MEEET (or P3MEEMT) increases, the dark (lower) phase can be assigned to P3MEEET (or P3MEEMT), while the bright (higher) phases can be assigned to PS. This assignment is confirmed by the STXM results presented below. (It is noted that these phases are not necessarily pure and are better regarded as P3MEEET-rich or P3MEEMT-rich and PS-rich phases.) As continuous P3MEEET (or P3MEEMT) phases are observed for the 10:6 (v/v), 11:5 (v/v), and 12:4 (v/v) compositions, these compositions were selected for further investigation and the preparation of corresponding porous films. These compositions will subsequently be referred to by their composition ratios of 10:6 (v/v), 11:5 (v/v), and 12:4 (v/v) OMIEC:PS. Figure 2g-i shows the porous samples produced for these blend compositions via selective dissolution in cyclohexane. Comparison with the AFM images of the corresponding blend samples, the previous bright (higher) regions now appear dark, suggesting the successful removal of PS, which is further confirmed by the STXM results presented below.

Scanning transmission X-ray microscopy was employed as a complementary technique with similar resolution to AFM but with chemical contrast afforded by near-edge X-ray absorption fine-structure (NEXAFS) spectroscopy. Figure 3a shows the

https://doi.org/10.1021/acsami.6c05714
ACS Appl. Mater. Interfaces 2026, 18, 30250–30268

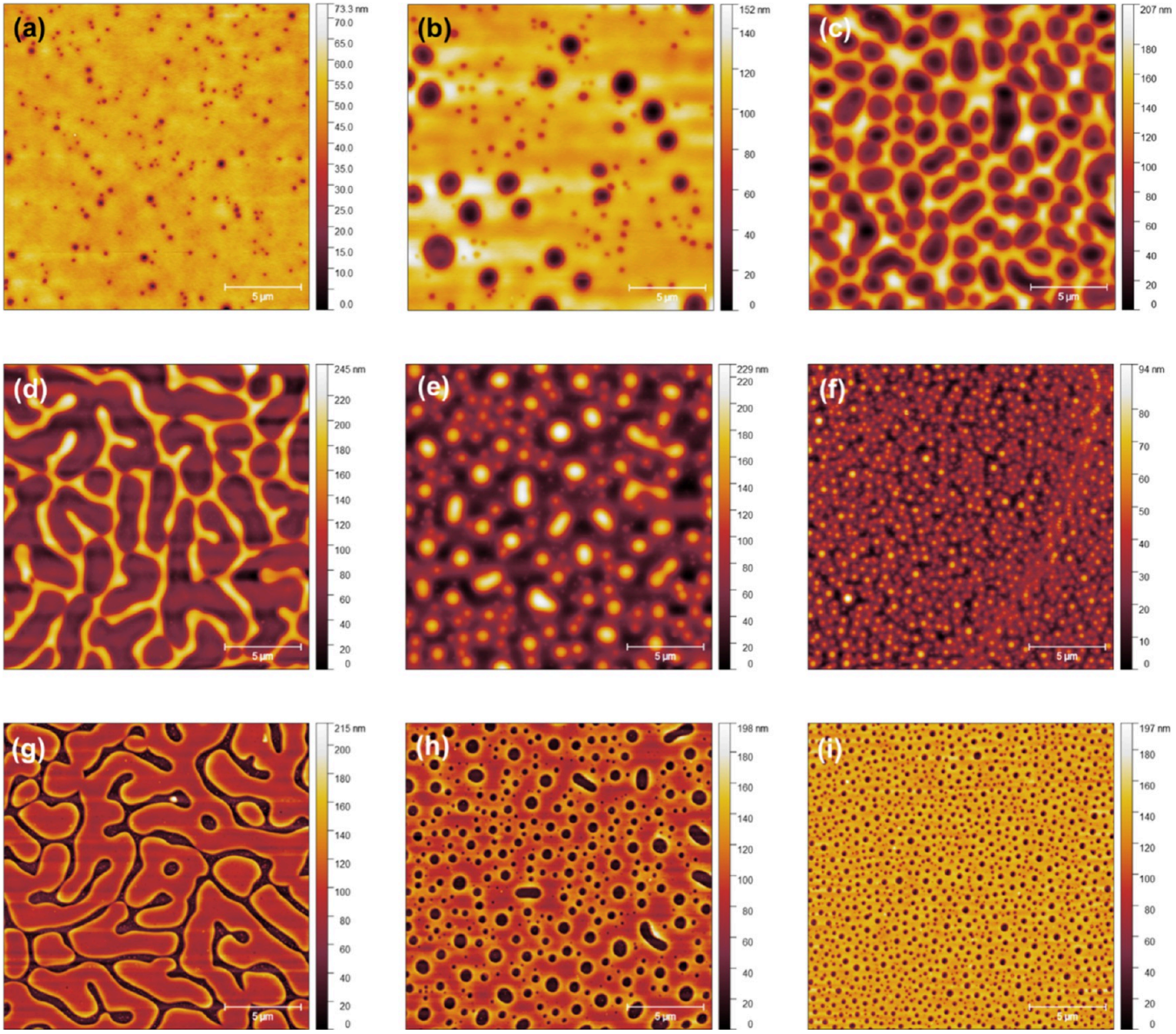

Figure 2. AFM height images (20 μm × 20 μm) of P3MEEET:PS samples with (a) 4:12 (v/v) blend; (b) 5:11 (v/v) blend; (c) 8:8 (v/v) blend; (d) 10:6 (v/v) blend; (e) 11:5 (v/v) blend; (f) 12:4 (v/v) blend; (g) 10:6 (v/v) porous; (h) 11:5 (v/v) porous; (i) 12:4 (v/v) porous. The scale bar is 5 μm.

reference NEXAFS spectra taken of neat samples, demonstrating that PS has a distinct chemical "fingerprint" to both P3MEEET and P3MEEMT. In particular, PS has a sharp peak at ∼285 eV associated with the pendant phenyl rings. P3MEEET and P3MEEMT have similar spectra as expected due to their similar chemistry. Figure 3b shows the STXM image of the 11:5 P3MEEET:PS blend (68.75% blend) taken at 284.75 eV, where PS preferentially absorbs (images taken at other energies are shown in the Supporting Information, Figures S2−S13). Dark regions therefore correspond to areas rich in PS, with the morphology consistent with that seen by AFM, consisting of enclosed PS-rich domains surrounded by a continuous P3MEEET-rich phase. Figure 3c shows the STXM image of the 11:5 P3MEEET:PS porous sample taken at 284.75 eV. Regions that appeared dark in the blend sample now appear bright, indicating PS has been removed from the sample. Calibrating the reference neat spectra to the absolute X-ray absorption cross sections of the samples (based on their chemical formula), it is possible to produce 1D line profiles of PS thickness, P3MEEET thickness, and total film thickness, Figure 3d,e. This was achieved by taking line scans where full NEXAFS spectra were taken at each point along the line and fitting each spectrum to a linear combination of the neat spectra. Figure 3d shows a line profile for the 11:5 P3MEEET:PS blend sample, which confirms that the enclosed regions are rich in PS and the continuous phase is rich in P3MEEET. Notably, there is a significant amount of P3MEEET detected in the PS-rich phase, while the P3MEEET-rich phase is essentially pure within experimental uncertainties. Examining the line profile of the 11:5 P3MEEET:PS porous sample, in Figure 3e (also in Figures S2−S13), all PS has been removed except for some small inclusions. Of note is that while there are holes that extend through the film where PS domains once were, there is also a residual P3MEEET wetting layer of ∼20 nm that partially blocks some of these holes. To further check for evidence of

https://doi.org/10.1021/acsami.6c05714
ACS Appl. Mater. Interfaces 2026, 18, 30250−30268

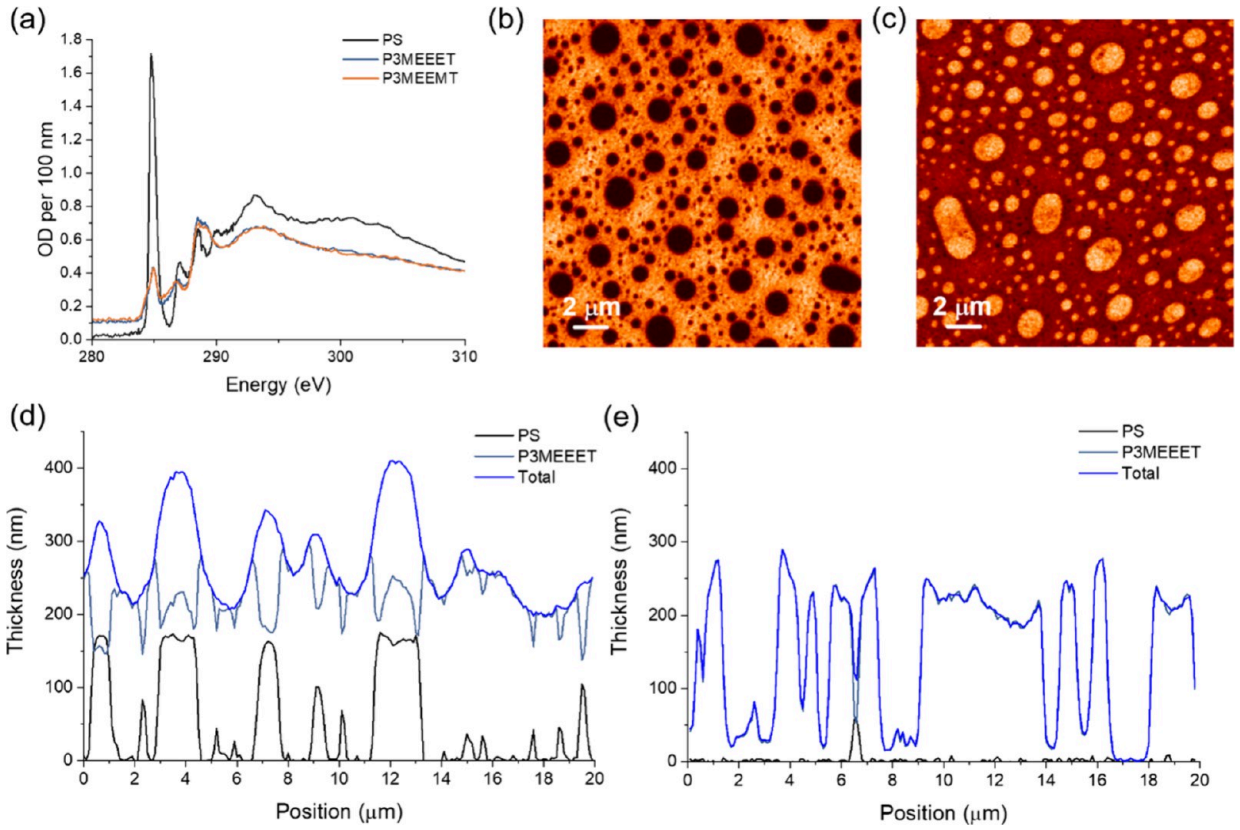

Figure 3. STXM of 11:5 P3MEEET:PS blend and porous samples: (a) transmission NEXAFS spectra of neat films; (b) transmission STXM image of 11:5 blend taken at 284.75 eV where PS selectively absorbs (PS-rich regions are dark); (c) transmission STXM image of 11:5 porous sample taken at 284.75 eV showing removal of PS; (d) line profile of 11:5 blend; and (e) line profile of 11:5 porous sample.

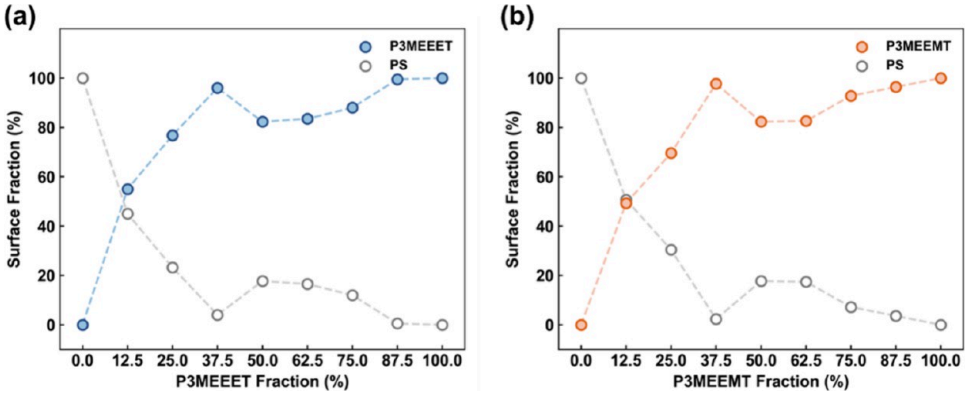

Figure 4. Surface composition at various blending ratio between (a) P3MEEET:PS and (b) P3MEEMT:PS.

vertical stratification, in particular at the top surface, surface-sensitive NEXAFS spectroscopy was next employed.

By performing electron-yield NEXAFS spectroscopy measurements on films in vacuum, surface sensitivity of a few nm (similar to X-ray photoelectron spectroscopy) can be achieved. The NEXAFS spectra of blends were measured and then fit with a linear combination of neat spectra to determine the surface composition of the blends. Note that NEXAFS spectroscopy measurements were performed with a mm-sized beam that averages over the lateral variations seen by STXM. Figure 4 plots the surface composition of the uppermost layer of the blend samples as a function of blend ratio (example fits are shown in Figure S14). For all compositions, an enrichment of P3MEEET or P3MEEMT is seen at the top surface. For example, the 4:12 blend with a P3MEEET volume fraction of 25% has a surface composition of ~75% P3MEEET. For compositions studied in devices, ranging between 10:6 (62.5%$_v$) and 12:4 (75%$_v$) more than 80% of the surface is covered by P3MEEET (or P3MEEMT). These results indicate that there is a thin (partial) capping layer of P3MEEET (or P3MEEMT) that also covers the laterally phase-separated PS-rich domains.

Optoelectronic Properties

The UV−vis spectra of P3MEEET and P3MEEMT with their respective blends and porous films are displayed in Figure 5a,b. The pure P3MEEET exhibits a major absorption peak at 505 nm, along with two further peaks at 550 and 600 nm. For blends and porous films, the major absorption peaks exhibit a

https://doi.org/10.1021/acsami.6c05714
ACS Appl. Mater. Interfaces 2026, 18, 30250−30268

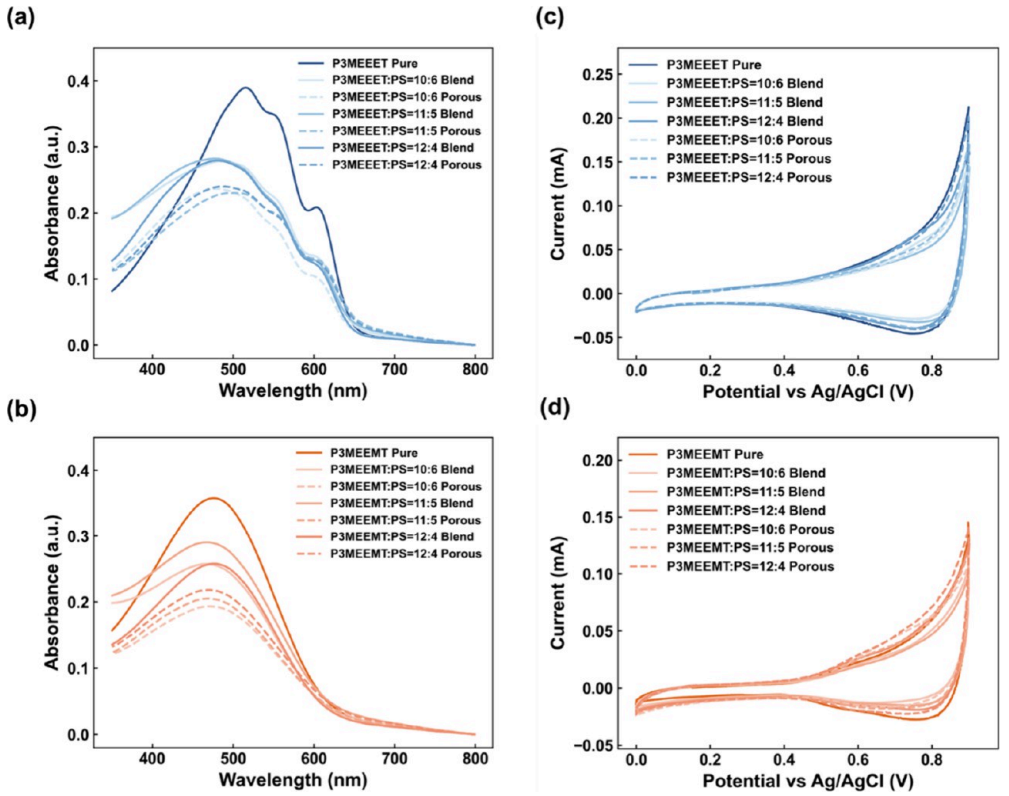

Figure 5. UV−vis spectra as thin films on glass of: (a) P3MEEET and (b) P3MEEMT both with its blend and porous series; Cyclic voltammogram of (c) P3MEEET and (d) P3MEEMT as thin films both with its blend and porous series on ITO in 0.1 M NaCl.

blue shift to the range of 490−500 nm, which suggests a reduction in local order upon addition of PS. This elevated apparent absorbance at lower wavelengths may also have a contribution from light scattering due to the rough surfaces of the blend and porous samples. In the P3MEEMT series, all of the pure, blend, and porous samples exhibit a single absorption peak at 485 nm, which implies reduced aggregation features compared to P3MEEET with P3MEEMT also exhibiting a larger optical gap than P3MEEET.

The cyclic voltammograms (CV) of both P3MEEET and P3MEEMT were next measured, along with their blends with PS and corresponding porous films in 0.1 M NaCl. Films of these samples were measured on conductive indium tin oxide (ITO) substrates with the voltage varied from 0 to 0.9 V vs Ag/AgCl to study the oxidation process and obtain the oxidation potentials (Figures 5c,d and S15), which remain below the potential where substantial water oxidation happens (~1.23 V). Three cycles were performed per sample, showing that no obvious irreversible changes or oxidation processes happened under high potentials (Figure S16). Comparing the P3MEEET and P3MEEMT series of samples, P3MEEET samples in general exhibit a slightly lower oxidation voltage (~0.42 V) compared to P3MEEMT samples (~0.47 V), with the geometry of the film (i.e., neat, blend, or porous) not substantially affecting the oxidation potential (see Table S1). Spectroelectrochemistry (SEC) experiments were also performed on these films to investigate changes in absorption during the electrochemical doping process (Figure S17). As for CV measurements, all films were deposited on ITO substrates with the applied potential varied from 0 to 0.9 V vs Ag/AgCl with 0.1 V increment. Examples of normalized SEC spectra with the OMIEC:PS ratio of 11:5 are shown in Figure 6a,b for both blends (top) and porous (bottom) samples for both P3MEEET and P3MEEMT. With increasing voltage, the ground state $\pi-\pi^*$ absorption of P3MEEET at λ = 505 nm gradually decreases accompanied by the emergence of a polaron peak at λ = 750 nm. This trend is seen for both blend and porous samples. Similarly, for the P3MEEMT samples, the ground state $\pi-\pi^*$ absorption at λ = 485 nm decreases with increasing potential alongside the growth of the polaron peak λ = 780 nm. Figure S19 shows the changes in the polaron and $\pi-\pi^*$ absorption peaks for each sample, which were obtained from their reduced SEC spectra (Figure S18). Example curves showing peak changes versus the applied potential are shown in Figure 6c for P3MEEET:PS = 11:5 and P3MEEMT:PS = 11:5. All samples demonstrate a doping onset at approximately 0.3−0.4 V and reach a maximum doping level at 0.8 V. At 0.9 V, the strength of the polaron peak and degree of ground state bleaching both decrease, more likely as a result of film delamination caused by the high applied potentials. Notably, when comparing the polaron peak variations at the maximum doping potential among the pure, blend, and porous samples (Figure 6d), it is obvious that the porous samples demonstrate markedly greater peak changes than the corresponding blends and pure samples in P3MEEMT at their highest doping stages, as also illustrated in Figure 6c. In P3MEEET, analogous behavior is observed; however, the difference of the polaron peaks between its blend and porous is less noticeable than that in P3MEEMT. This difference indicates an increased doping level in porous films, suggesting that these films have superior ion storage capabilities compared to blends and pure films, consistent with increased ion injection from the sides. Consequently, porous samples demonstrate superior ion storage in comparison to their corresponding blends and

https://doi.org/10.1021/acsami.6c05714
ACS Appl. Mater. Interfaces 2026, 18, 30250−30268

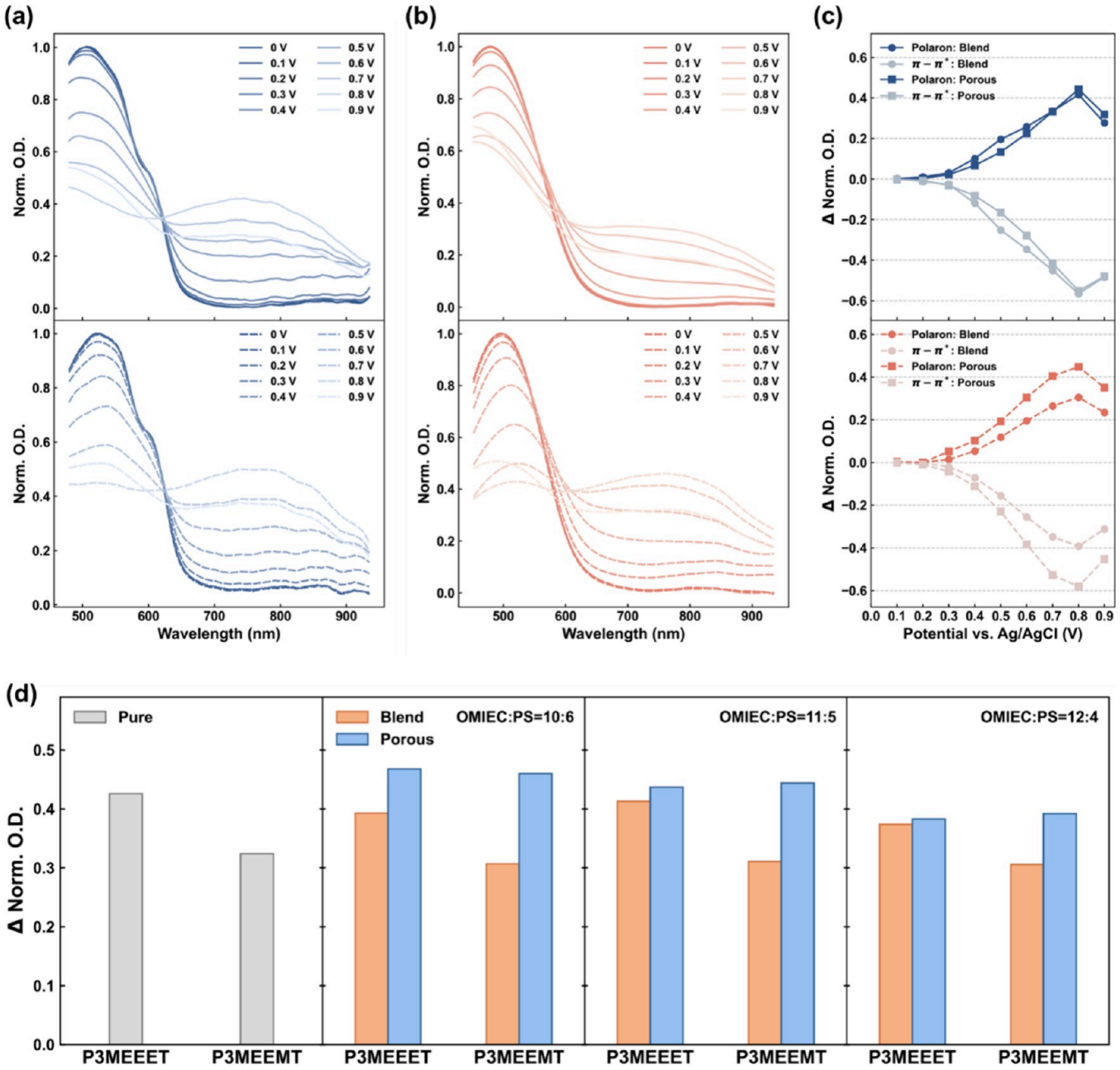

Figure 6. An example comparison of SEC spectra between (a) P3MEEET:PS = 11:5 blend (top) and porous (bottom) samples; (b) P3MEEMT:PS = 11:5 blend (top) and porous (bottom) samples; (c) Changes in the intensities of polaron peak and π–π* absorption peaks obtained from the difference spectra (Figure S18); (d) Reference maximum polaron peak changes (0.8 V) of pure P3MEEET and P3MEEMT, with comparative analysis of maximum polaron peak changes at 0.8 V in blend and porous samples across different blending ratios with PS.

pure samples, with P3MEEMT samples showing a strong enhancement compared to P3MEEET samples.

OECT Performance

The OECT performance of all P3MEEET and P3MEEMT systems (pure, blend, and porous) were evaluated utilizing an Ag/AgCl pellet as the gate and a 0.1 M NaCl aqueous solution as the electrolyte. Figure 7a,b compare the transfer characteristics and transconductance for the P3MEEET blend and porous systems, while Figure 7d,e compare the same for the P3MEEMT blend and porous systems. Gate voltages ranging from 0 to −0.8 V were applied while the drain voltage was set at −0.8 V. In blend systems, both P3MEEET and P3MEEMT demonstrate that the inclusion of PS results in a substantial enhancement of their transconductance. The P3MEEET:PS and P3MEEMT:PS blends with a ratio of OMIEC:PS of 11:5 exhibit superior performance compared to the other blends and pure samples. In particular, for the P3MEEET series, the film thickness normalized transconductance increases from 1.70 S/cm for the neat sample to 2.76 S/cm for the 11:5 blend, while for the P3MEEMT series the transconductance increases from 1.05 S/cm for the neat sample to 1.95 S/cm for the 11:5 blend (see Table 1 for a summary of all performance parameters). Indeed, the device output, illustrated in Figure S20, demonstrates that the P3MEEET/P3MEEMT:PS = 11:5 blend samples yield the maximum saturation drain current (I_D) at −0.8 V for all systems. However, for the porous systems, the transconductance exhibits a systematic decrease with decreas-

https://doi.org/10.1021/acsami.6c05714
ACS Appl. Mater. Interfaces 2026, 18, 30250−30268

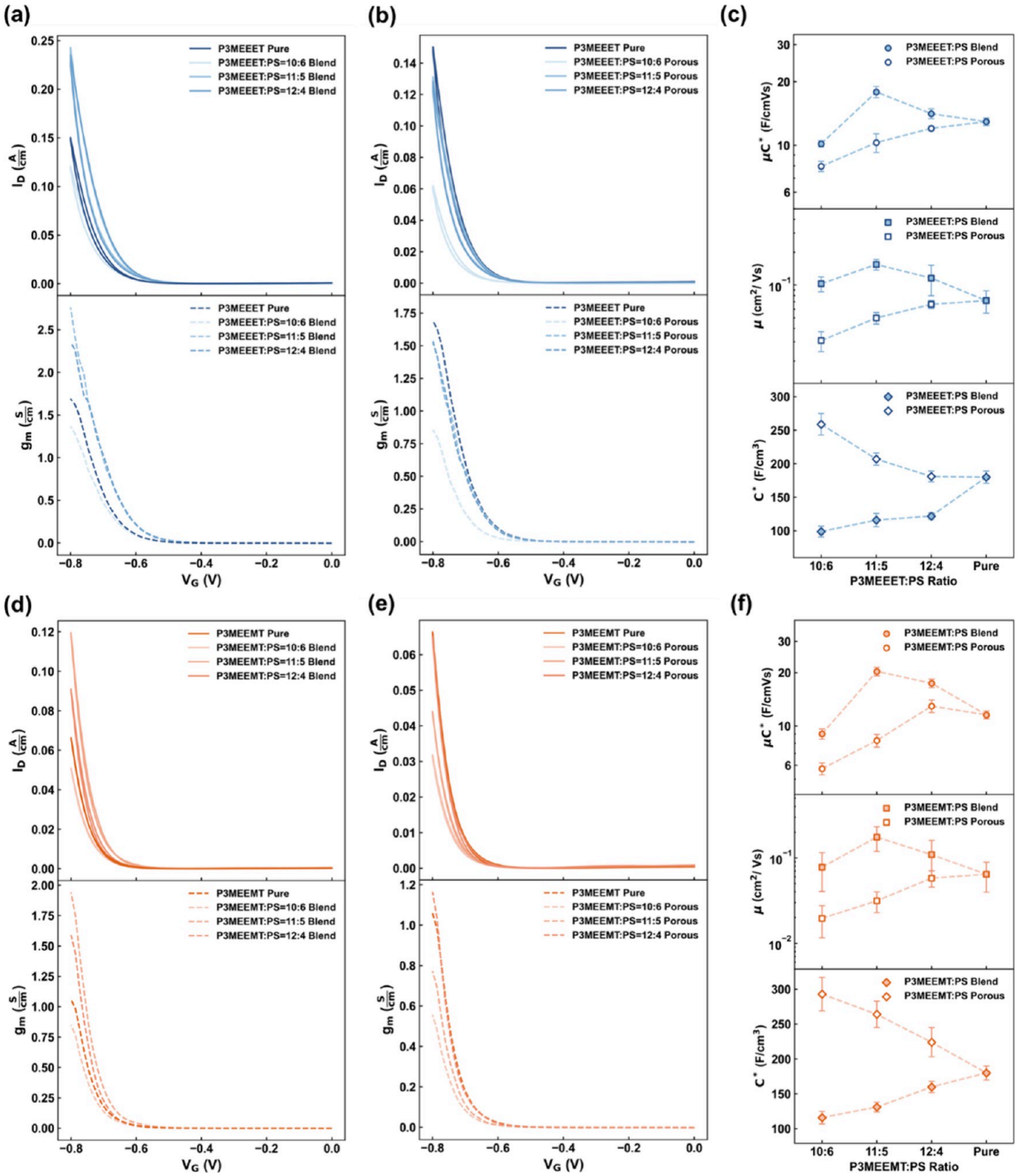

Figure 7. Transfer curves (top) and g_m (bottom) between pure and (a) blend (b) porous P3MEEET samples across different blending ratio of PS; (c) Figure of merit (top), mobility (middle) and effective volumetric capacitance (bottom) of P3MEEET blend and porous samples across different blending ratios with PS; Transfer curves (top) and g_m (bottom) between pure and (d) blend (e) porous P3MEEMT samples across different blending ratios of PS; (f) Figure of merit (top), mobility (middle), and effective volumetric capacitance (bottom) of P3MEEMT blend and porous samples across different blending ratios with PS.

ing OMIEC content (corresponding to an increase in pore volume). For the poorest performer, P3MEEET/P3MEEMT:PS = 10:6 porous samples, the transconductance decreases to half that of corresponding pure samples.

https://doi.org/10.1021/acsami.6c05714
ACS Appl. Mater. Interfaces 2026, 18, 30250−30268

Table 1. Summary of All OECT Parameters[a]

polymer	$g_{m,max}$ [S/cm][b]	μC^* [F/cmVs][c]	μ [cm^2/(V s)][d]	C^* [F/cm^3][e]	τ_{on} [s][f]
P3MEEET pure	1.70	13.0 ± 0.5	0.07 ± 0.02	180 ± 9	1.5 ± 0.1*
P3MEEET:PS = 10:6 blend	1.37	10.2 ± 0.4	0.10 ± 0.02	99 ± 8	0.093 ± 0.007
P3MEEET:PS = 11:5 blend	2.76	18 ± 1	0.15 ± 0.02	120 ± 10	0.05 ± 0.02
P3MEEET:PS = 12:4 blend	2.35	14.1 ± 0.8	0.12 ± 0.04	122 ± 5	0.45 ± 0.06*
P3MEEET:PS = 10:6 porous	0.85	8.0 ± 0.4	0.031 ± 0.006	260 ± 20	2 ± 1*
P3MEEET:PS = 11:5 porous	1.52	10 ± 1	0.050 ± 0.006	207 ± 9	1.9 ± 0.4*
P3MEEET:PS = 12:4 porous	1.53	12.0 ± 0.3	0.067 ± 0.006	181 ± 8	1.6 ± 0.3*
P3MEEMT pure	1.05	11.6 ± 0.6	0.06 ± 0.02	180 ± 10	0.19 ± 0.06
P3MEEMT:PS = 10:6 blend	0.85	9.0 ± 0.6	0.08 ± 0.04	116 ± 9	0.40 ± 0.06
P3MEEMT:PS = 11:5 blend	1.95	20 ± 1	0.18 ± 0.06	131 ± 7	0.36 ± 0.04
P3MEEMT:PS = 12:4 blend	1.59	17 ± 1	0.11 ± 0.05	160 ± 8	0.28 ± 0.06
P3MEEMT:PS = 10:6 porous	0.55	5.7 ± 0.4	0.020 ± 0.008	290 ± 20	0.17 ± 0.03
P3MEEMT:PS = 11:5 porous	0.77	8.3 ± 0.7	0.031 ± 0.009	260 ± 20	0.18 ± 0.03
P3MEEMT:PS = 12:4 porous	1.12	13 ± 1	0.06 ± 0.01	220 ± 20	0.17 ± 0.02

[a]Data are presented as mean ± standard deviation, based on measurements from 5 individual devices for each composition and architecture. [b]The maximum transconductance is extracted from the first-order derivative of the forward transfer curves. [c]The product of μC^* is derived from the transconductance curves by applying Bernard's model.[65] [d]The mobility μ is decoupled by dividing μC^* by the volumetric capacitance C^* [e]The volumetric capacitance C^* was measured by EIS. [f]For transient response, the * denotes the "spike and recovery" behavior.

The figures of merit (μC^*) were derived from their respective g_m to assess the overall performance of their mixed ionic-electronic conductance (see Figure S21). Subsequently, they were decoupled to evaluate electronic mobility and ionic storage independently by determining the effective volumetric capacitance from EIS (see Figure S22), with μC^*, μ, and C^* plotted as a function of composition and sample type in Figure 7c for the P3MEEET series and in Figure 7f for the P3MEEMT series. From these plots, it can be seen that the incorporation of PS in the blend systems for both the P3MEEET and P3MEEMT series enhances the overall device performance. The optimal performers (P3MEEET/P3MEEMT:PS = 11:5) exhibit a notable improvement in μC^* compared to their pure samples: for the P3MEEET:PS = 11:5 blend, μC^* increases from 13.0 ± 0.5 F/cmVs for the neat sample to 18 ± 1 F/cmVs for the P3MEEET:PS = 11:5 blend, while μC^* increases from 11.6 ± 0.6 F/cmVs for the neat sample to 20 ± 1 F/cmVs for the P3MEEMT:PS = 11:5 blend. In porous systems, the figures of merit show systematically decreasing trends with increasing pore volume for both the P3MEEET and P3MEEMT series, decreasing to 8.0 ± 0.4 F/cmVs for the P3MEEET:PS = 10:6 porous sample and to 5.7 ± 0.4 F/cmVs for the P3MEEMT:PS = 10:6 porous sample. This observation indicates that the presence of pores adversely impacts the overall mixed ionic-electronic performance of these two polymer types.

Upon decoupling μC^* into separate μ and C^* values by measuring C^* using EIS, it is observed that the electronic mobility (μ) exhibits an upward trend with the incorporation of PS until a ratio of P3MEEET/P3MEEMT:PS = 11:5, followed by a slight decline upon further increasing the PS amount to the ratio of P3MEEET/P3MEEMT:PS = 10:6. In the P3MEEET series, for the top performer, P3MEEET:PS = 11:5, the mobility is enhanced to 0.15 ± 0.02 cm^2/(V s) from 0.07 ± 0.02 cm^2/(V s) for the neat sample, representing a 2-fold increase. For P3MEEMT, the mobility is enhanced by 2.5 times in the optimum blend (P3MEEMT:PS = 11:5), up to a value of 0.18 ± 0.06 cm^2/(V s) from a value of 0.06 ± 0.03 cm^2/(V s) for the neat sample. On the other hand, the effective volumetric capacitance (C^*) demonstrates monotonic decreases with increasing PS content in the blend system; for the sample with a P3MEEET:PS ratio of 10:6, C^* is reduced to 99 ± 8 F/cm^3 down from a value of 180 ± 9 F/cm^3 for the pure sample. The P3MEEMT:PS = 10:6 blend sample exhibits the lowest C^* value among all blend samples, with a value of C^* = 120 ± 10 F/cm^3, compared to a value of C^* = 180 ± 10 F/cm^3 for the neat P3MEEMT sample. In contrast, the addition of pores is found to enhance the effective volumetric capacitance. As porosity increases, effective volumetric capacitance grows correspondingly. The P3MEEET/P3MEEMT:PS = 10:6 porous samples in particular exhibit a notable increase in effective volumetric capacitance, increasing to C^* = 260 ± 20 F/cm^3 for the P3MEEET series to C^* = 290 ± 20 F/cm^3 for the P3MEEMT series. These findings regarding the C^* of the porous samples were also consistent with the SEC results, indicating that the incorporation of pores improves the ability of ion storage. We also observe a decline in the mobility upon increasing the proportion of pores from P3MEEET/P3MEEMT:PS = 11:5 to 10:6, likely due to the increase in discontinuity of the film. As illustrated in Figure 3, the addition of PS and pores can induce discontinuities that obstruct the pathway of charge carrier transport, resulting in adverse effects on electronic transport.

QCM analysis was performed to examine the influence of blending with PS, along with the influence of the porous structure, on the swelling behavior of P3MEEET and P3MEEMT. Films were spin-coated onto crystal sensors and examined on the QCM while being exposed to an aqueous 0.1 M NaCl solution. Samples with a ratio of P3MEEET/P3MEEMT:PS = 11:5 films were selected, and changes in their oscillation frequency and their translated volume changes are recorded illustrated in Figure S23, while their swelling percentages are summarized in Figure S24. The P3MEEET:PS = 11:5 blend sample showed a reduced swelling of 5% compared to the reference neat sample (12%), while the corresponding 11:5 porous sample showed an increased swelling percentage to 20%. In the P3MEEMT series, the 11:5 blend sample had a diminished swelling of 15% relative to the neat P3MEEMT sample (29%), whereas the 11:5 porous sample showed an increased swelling percentage of 41%. These findings indicate that the incorporation of PS mitigates swelling effects by restricting water penetration, while the

https://doi.org/10.1021/acsami.6c05714
ACS Appl. Mater. Interfaces 2026, 18, 30250−30268

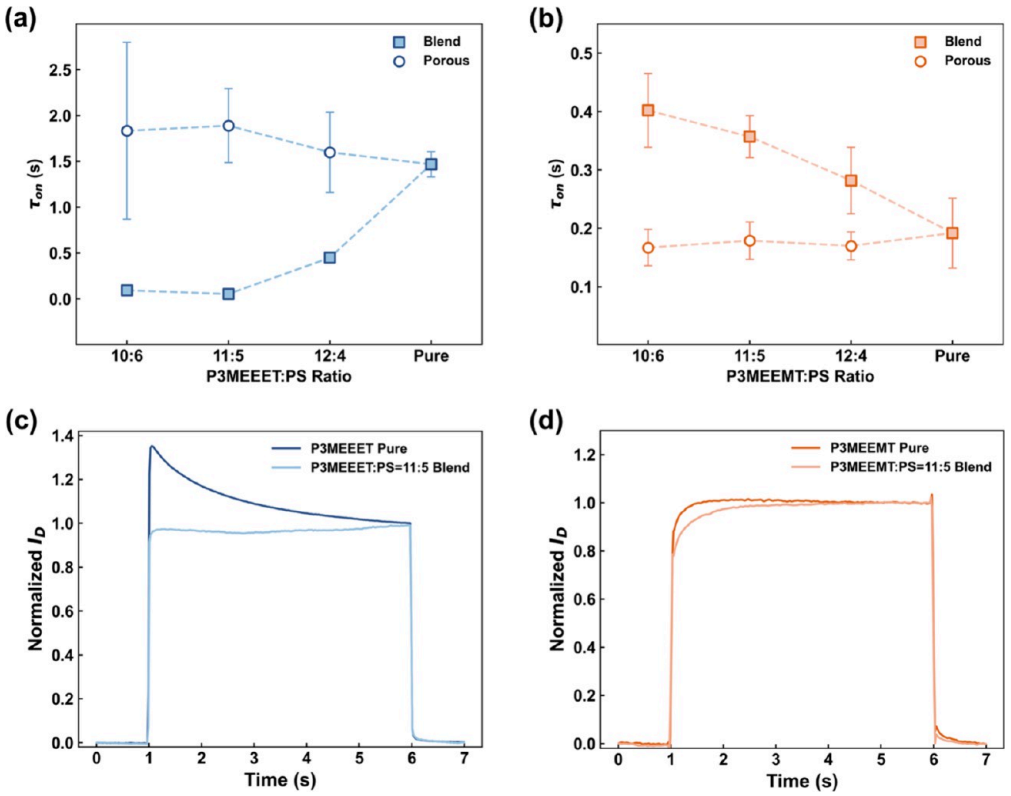

Figure 8. Summarized switch-on time of (a) P3MEEET and (b) P3MEEMT blend and porous samples across different blending ratios with PS; Comparison of the transient response between (c) P3MEEET pure and P3MEEET:PS = 11:5 blend and (d) P3MEEMT pure and P3MEEMT:PS = 11:5 blend.

incorporation of pores enhances swelling by increasing the areas accessible for water penetration from the sides. This finding also indicates that the porous samples exhibit heightened sensitivity during the hydration process, particularly for P3MEEMT. This enhanced swelling may facilitate the entrance of ions into the film during the initial doping stage, thereby potentially enhancing ion storage, consistent with the SEC results and values of the effective volumetric capacitance.

The transient response of an OECT reflects the coordination of mixed ionic-electronic transport in the device. The transient response of the OECT devices was characterized by applying a −0.8 V drain voltage with a −0.8 V gate voltage impulse for 5 s to determine the switch-on time, see Figure S25 for the full data set. Transient response typically exhibits two behavioral types: "monotonic relaxation," characterized by ionic charging occurring more slowly than electronic transport, and "spike and recovery," which arises when there is latency in electronic transport. Figure 8c,d illustrates the switch-on time, τ_{on}, for all pure, blend, and porous samples of P3MEEET and P3MEEMT (see Figure S26 for example fits used to determine τ_{on} and see the Experimental Section for how τ_{on} is defined and determined). These findings are summarized in Table 1, where an asterisk indicates spike and recovery behavior. We observe a notable difference in the transient characteristics between P3MEEET and P3MEEMT. In the P3MEEET series, both pure and porous samples exhibit a pronounced spike and recovery behavior, indicating accelerated ionic transport. The recorded latency values were found to increase slightly with increasing porosity. In the P3MEEET:PS = 11:5 porous sample, the switch-on time is 1.9 ± 0.4 s, which is slightly increased, but comparable to 1.7 ± 0.1 s for the pure sample, likely due to the side injection boosting the ionic process. Conversely, the incorporation of PS may reduce the latency caused by electronic transport, progressively transitioning its behavior to monotonic relaxation. (Figure 8c) This allows for optimization of the precise orchestration between ionic and electronic processes at a ratio of P3MEEET:PS = 11:5 with τ_{on} = 0.05 ± 0.01 s. In the P3MEEMT series, all pure, blend, and porous films exhibit a monotonic relaxation behavior (Figure 8d); as the amount of PS in the blend increases, the ionic latency rises monotonically from 0.19 ± 0.06 s in the pure sample to 0.40 ± 0.06 s. Unlike the P3MEEET series, the incorporation of pores for a system where there is already monotonic relaxation behavior can expedite the ionic response, thereby reducing latency in relation to the electronic response and slightly reducing the switch-on time of the device.

Structural Characterization

To investigate the impact of electrochemical doping on film microstructure and its potential effects on electronic transport, grazing incidence wide-angle X-ray scattering was performed. Figure 9a,c illustrate the 2D GIWAXS patterns of pure P3MEEET, P3MEEMT, and PS, while the 2D GIWAXS patterns of additional blends and porous films are depicted in Figure S27; the corresponding linecuts in both in-plane and out-of-plane directions are presented in Figure 9d−g. All relevant GIWAXS indices are listed in Table S2. The 2D GIWAXS figures indicate that both P3MEEET and P3MEEMT, along with their blend and porous films, display mixed orientations, including both face-on and edge-on configurations, whereas PS is characterized by an amorphous microstructure with only broad, diffuse scattering features as

https://doi.org/10.1021/acsami.6c05714
ACS Appl. Mater. Interfaces 2026, 18, 30250−30268

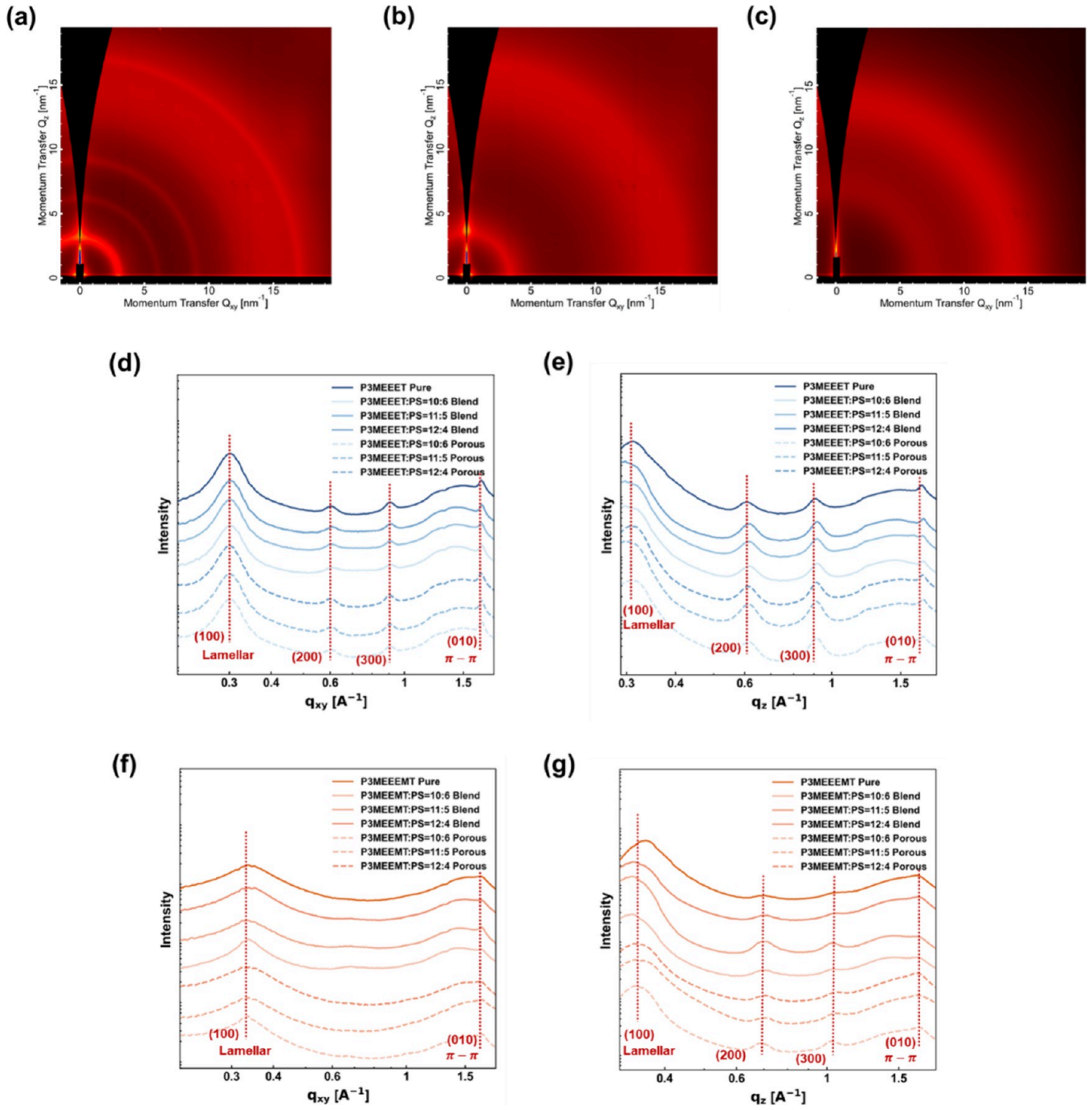

Figure 9. 2D GIWAXS reciprocal space maps of (a) P3MEEET pure, (b) P3MEEMT pure, and (c) PS pure; reduced 1D GIWAXS map for (d) in-plane and (e) out-of-plane of P3MEEET pure, blend, and porous samples across different blending ratios with PS; reduced 1D GIWAXS map for (f) in-plane and (g) out-of-plane of P3MEEMT pure, blend, and porous samples across different blending ratios with PS.

previously reported.[57,58] The 1D linecuts in Figure 9d–g reveal both lamellar stacking peaks and π-π stacking peaks in the in-plane and out-of-plane directions for the P3MEEET and P3MEEMT series. The linecuts also evidence that these peaks are still present in the blend and porous samples, indicating that the incorporation of PS and the selective dissolution of PS to form porous samples does not significantly alter the thin film crystallinity.

The GIWAXS data were then further analyzed by peak fitting to obtain a detailed comparison between samples. As shown in Figure 9d,e, the (100) peaks appear at approximately q_{xy} = 0.30 Å^{-1} and q_z = 0.31 Å^{-1} for all pure, blend, and porous films in the P3MEEET series; while in the P3MEEMT series, the (100) peaks were observed at approximately q_{xy} = 0.34 Å^{-1} and q_z = 0.34 Å^{-1} (Figure 9f,g). A weak π–π stacking peak is detected at around q = 1.67 Å^{-1} in both the in-plane and out-of-plane directions for both types of polymer. The d-spacings were determined from the (100) lamellar peak via the equation $d = \frac{2\pi}{q}$, to be approximately d = 20.5 Å for the P3MEEET series and about 18.5 Å for the P3MEEMT series, indicating that the P3MEEMT blends exhibit a consistently denser lamellar packing consistent with the short side chain length of

https://doi.org/10.1021/acsami.6c05714
ACS Appl. Mater. Interfaces 2026, 18, 30250–30268

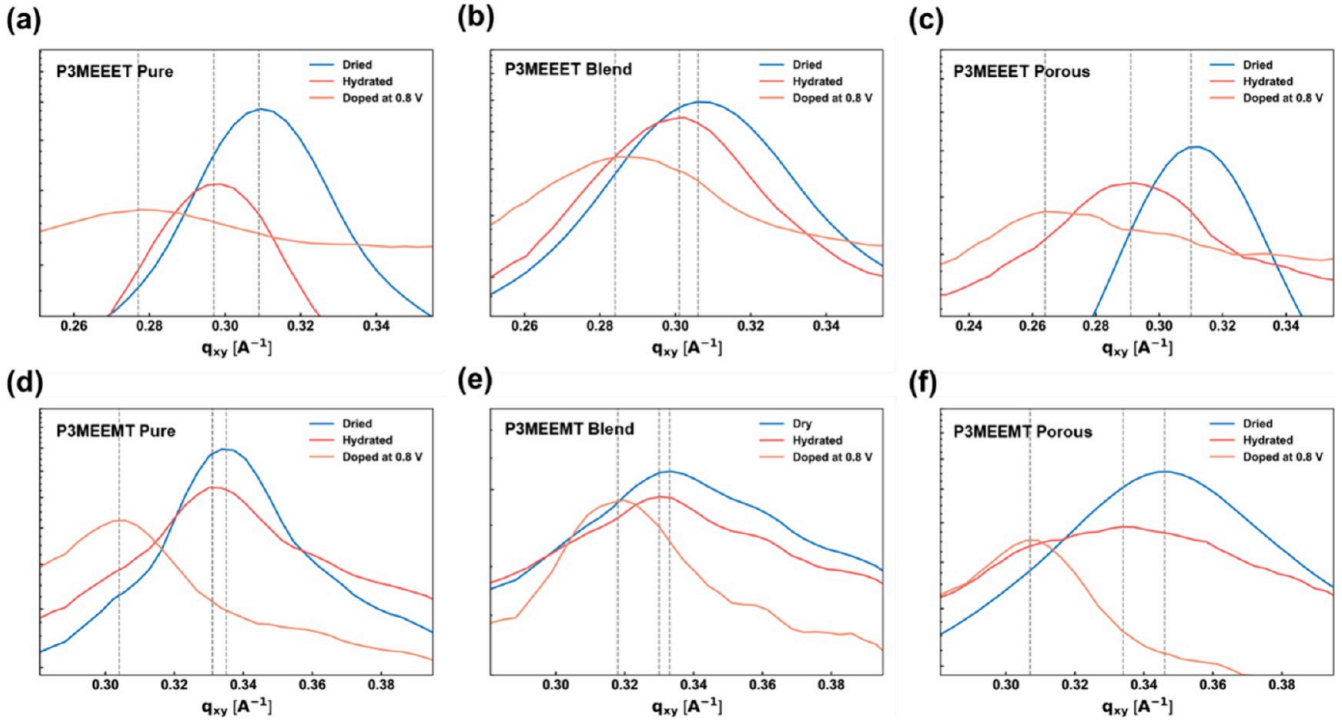

Figure 10. In-plane (100) peak evolution during in situ GIWAXS measurements of (a) P3MEEET pure, (b) P3MEEET:PS = 11:5 blend, (c) P3MEEET:PS = 11:5 porous, (d) P3MEEMT pure, (e) P3MEEMT:PS = 11:5 blend, and (f) P3MEEMT:PS = 11:5 porous films, recorded during the transition from the dry to the passive and active swelling states.

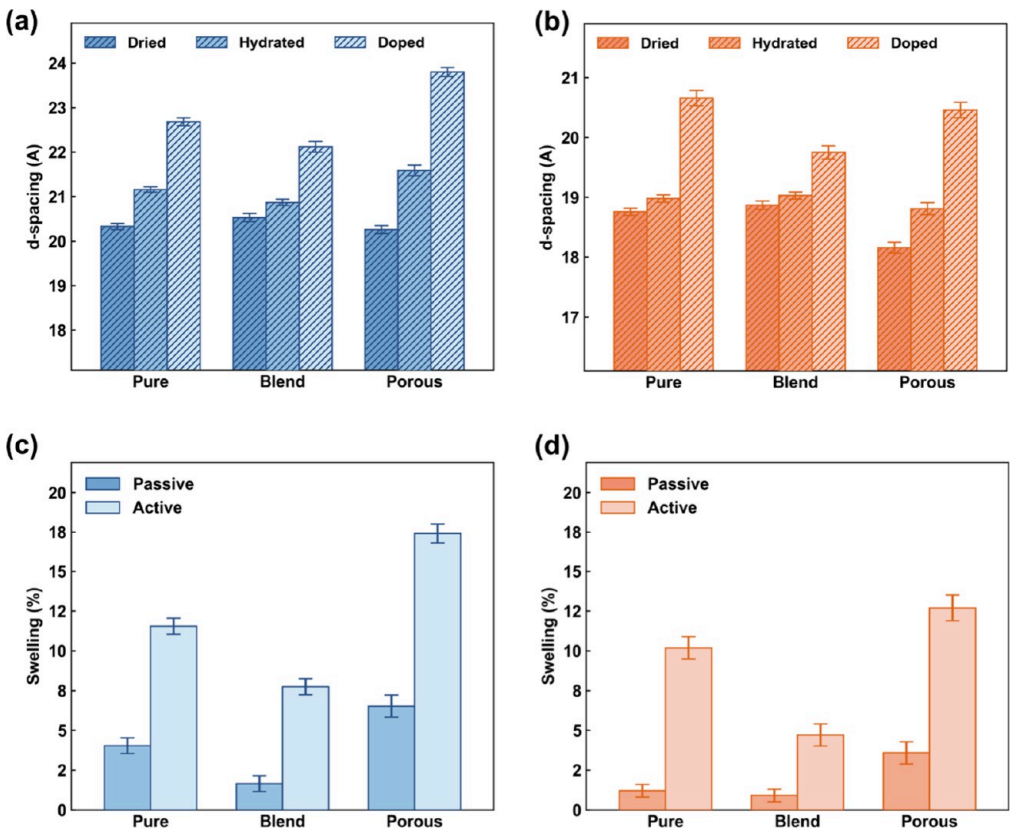

Figure 11. Comparisons in *d*-spacing of the 100 peaks from Figure 10 between the pure, 11:5 blend, and 11:5 porous samples in (a) P3MEEET series and (b) P3MEEMT series; and comparisons between passive and active swellings in crystallized domains of (c) P3MEEET series and (d) P3MEEMT series.

https://doi.org/10.1021/acsami.6c05714
ACS Appl. Mater. Interfaces 2026, 18, 30250−30268

P3MEEMT. The P3MEEET series has distinct (200) and (300) lamellar peaks in both in-plane and out-of-plane directions, whereas these peaks are absent in the in-plane direction for the P3MEEMT series. This observation indicates that the P3MEEET series demonstrates a mixed orientation without preference, while the P3MEEMT series exhibits a mixed orientation but with a preferential edge-on orientation. Differences in microstructure can be studied through quantification of the peak fwhm, enabling determination of the coherence length, which is influenced by crystallite size and disorder, with a larger coherence length generally reflecting larger, and/or more ordered crystals. As shown in Table S2, the coherence length, calculated from the peak fwhm, of the P3MEEET series (approximately 245 Å at the in-plane direction and 190 Å at the out-of-plane direction) is larger than that of the P3MEEMT series (approximately 100 Å at the in-plane direction and 145 Å at the out-of-plane direction), suggesting a higher degree of crystalline order in the P3MEEET series relative to the P3MEEMT series, which has also been discussed in previous work by Schmode et al.[31]

We further conducted GIWAXS experiments during electrochemical doping (in situ) on the pure, 11:5 blend, and 11:5 porous films within both the P3MEEET and P3MEEMT series to examine the lattice expansion in the crystalline domains during hydration and doped stages. The experiments were performed utilizing a rolling drop configuration as described by Flagg et al.[66] In brief, samples were prepared on gold-coated silicon wafers with a silver-coated glass slide used to blade-coat a thin film of the electrolyte. This silver-coated glass slide also serves as an electrode, with a voltage applied between the blade and the gold-coated substrate acting to electrochemically gate the film. As the electrolyte layer obscures the X-ray beam, as the electrolyte film recedes/dries, there is a small window in time where there is enough electrolyte to electrochemically gate the sample but it is thin enough to allow the X-ray beam to be transmitted for investigation of the polymer film. GIWAXS images were measured as a function of time during this transition from completely swollen to dry, allowing for this window to be captured. Experiments were performed with applied voltage, corresponding to electrochemical doping, and without applied voltage, corresponding to swelling/hydration only. Figure 10 illustrates that in both polymer types the porous films demonstrate a more significant peak shift than the pure films during hydration and doping. Conversely, the blends exhibit a reduced peak shift during these stages. This observation implies that the incorporation of PS could reduce lattice expansion during hydration and doping, while the presence of pores could promote lattice expansion. Figure 11a,b illustrates the *d*-spacing calculated from the (100) peak positions during the dried, hydrated, and doped stages. The data indicate that the *d*-spacing increases during the swelling process, with active swelling demonstrating a more significant lattice expansion, suggesting that ion insertion from the electrolytes facilitates greater expansion of the crystallized domains. In blends of P3MEEET and P3MEEMT, the *d* spacings varied less than in the pure samples, while the porous samples exhibited greater enhancement than their corresponding pure samples. This indicates that the incorporation of PS could inhibit lattice expansion during both hydration and doping stages, whereas the introduction of pores facilitates an increased capacity for water and ion insertion, thereby disrupting the crystallized domains more significantly than that in the pure samples.

The percentage expansion of the crystalline domains along the (100) direction was determined from the change in *d*-spacing, as illustrated in Figure 11c,d. Our observations indicate that P3MEEET exhibits greater expansion of crystallites than P3MEEMT across pure, blended, and porous films during both passive and active swelling, suggesting that the crystalline regions in P3MEEET are less resistant to swelling than those in P3MEEMT. Table 2 illustrates that during the passive swelling phase, the crystalline components in the neat P3MEEET:PS and P3MEEMT:PS blend films exhibit expansions of 1.7 and 0.9%, respectively, which is lower than their corresponding pure samples (4.0% for P3MEEET Pure and 1.2% for P3MEEMT Pure). Conversely, in porous samples, the crystalline components exhibited enhanced expansion, measuring 6.5% for P3MEEET and 3.6% for P3MEEMT. In active swelling, all films demonstrated an increased expansion of crystallites relative to passive swelling: Crystallites in P3MEEET were found to expand by 11.6% in the neat film, by 7.8% in the blend with PS, and by 17.4% in the porous sample. For P3MEEMT samples, crystallites in the neat sample were found to swell by 10.2%, by 4.7% in the blend, and by 12.7% in the porous sample. These results indicate that during active swelling, the inclusion of PS could still effectively inhibit swelling of the film; nevertheless, the pores could intensify swelling in the crystalline domains. This outcome further indicates that, during active swelling, the porous samples possess a greater potential to facilitate ion injection into the films, hence enhancing ionic storage, whereas the blends exhibit the opposite, consistent with the SEC data presented in Figure 6d. Upon comparison with the prior QCM results depicted in Figure S24, it is evident that the overall swelling in the P3MEEMT series is greater, but the swelling of the crystalline domains demonstrates the opposite, indicating that P3MEEMT contains a higher proportion of amorphous domains than P3MEEET, which is also consistent with the UV−vis measurements. The passive swelling of the crystalline domains is considerably less than that observed from QCM, suggesting that the majority of swelling occurs in amorphous regions, which may isolate the crystalline domains and consequently hinder charge transport in OECT devices, thereby diminishing carrier mobilities and the overall device performance. These results are in agreement with the mechanistic framework proposed by Ginger and co-workers,[43] further substantiating the role of amorphous domain swelling in limiting electronic transport.

Table 2. Comparisons of Swelling from In Situ GIWAXS and QCM

polymer	passive swelling from in situ GIWAXS (%)	active swelling from in situ GIWAXS (%)	passive swelling from QCM (%)
P3MEEET pure	4.0 ± 0.5	11.6 ± 0.5	12 ± 1
P3MEEET:PS = 11:5 blend	1.7 ± 0.5	7.8 ± 0.5	5 ± 0.5
P3MEEET:PS = 11:5 porous	6.5 ± 0.7	17.4 ± 0.6	20 ± 1
P3MEEMT pure	1.2 ± 0.4	10.2 ± 0.7	29 ± 2
P3MEEMT:PS = 11:5 blend	0.9 ± 0.4	4.7 ± 0.7	15 ± 1
P3MEEMT:PS = 11:5 porous	3.6 ± 0.7	12.7 ± 0.8	42 ± 3

https://doi.org/10.1021/acsami.6c05714
ACS Appl. Mater. Interfaces 2026, 18, 30250−30268

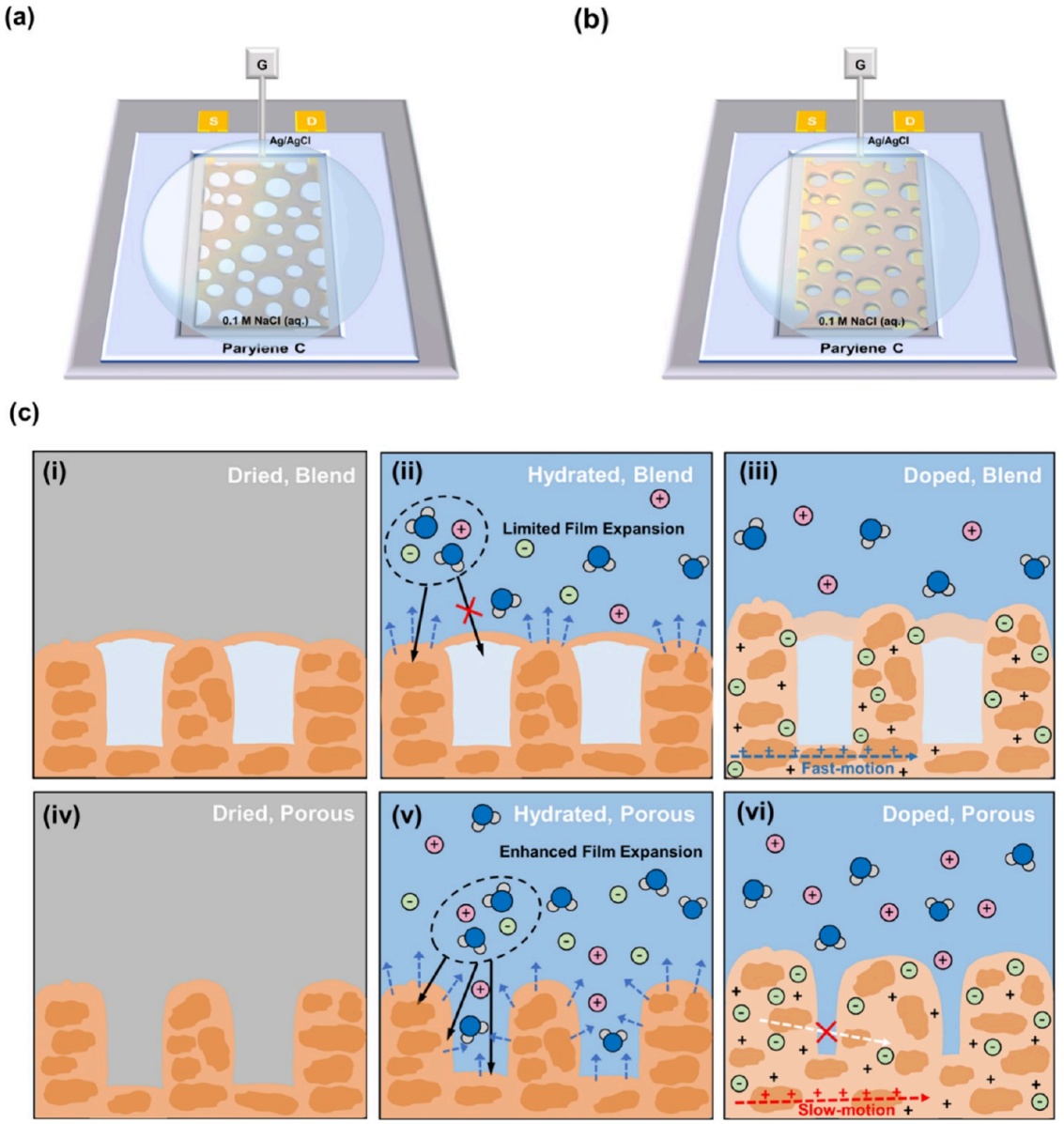

Figure 12. Schematic representation of OECT device with (a) blend films and (b) porous films. (c) Side view of the evaluation of the film in dried, hydrated and doped stages.

Mechanism of Mixed Ionic-Electronic Transport in Blend and Porous Films

To consolidate our findings, we proposed a mechanism for the film changes in mixed ionic-electronic transport during device operation. Figure 12a,b presents a schematic illustration of the device. Figure 12c(i) illustrates that the results of AFM and STXM indicate a pronounced lateral and vertical phase separation between the active polymers (P3MEEET or P3MEEMT) and PS. In the porous films, not only is the bulk PS phase removed, but the P3MEEMT/P3MEEET capping layer is removed along with it (Figure 12c (iv)). The results from QCM and in situ GIWAXS indicate that blend films inhibit swelling, while porous films promote it. When blend films are exposed to the electrolyte, the incorporation of PS appears to restrict swelling of the underlying active polymers by reducing their exposure to the electrolyte (Figure 12c(ii)). Conversely, in porous films, the underlying material expands the contact areas with the electrolyte after the PS is removed, resulting in increased swelling and enhanced permeability to ions and water molecules (Figure 12c(v)). During the doping stage, some active polymers in blend films are shielded by PS, which prevents further swelling and enhances electronic transport mobility. The swelling in the amorphous regions is diminished, leading to reduced separation between crystallized areas due to the limited ion and water injection zones. This enhancement facilitates the motion of charge carriers, improving the figure of merit and mobilities, as indicated in Figure 12c(iii) and suggested in Figure 5. Conversely, as indicated in Figure 7 and the combined result of QCM and in situ GIWAXS, porous films have greater exposure to the electrolyte, facilitate swelling, which results in increased expansion of the amorphous regions and separation of the crystalline domains, ultimately impeding the movement of charge carriers within the film. Furthermore, the loss of the P3MEEMT/P3MEEET capping layer leads to a reduction in connectivity, creating

https://doi.org/10.1021/acsami.6c05714
ACS Appl. Mater. Interfaces 2026, 18, 30250−30268

additional barriers for electronic transport throughout the film (Figure 12c(vi)).

CONCLUSIONS

In summary, we have demonstrated a morphology-engineering strategy to tune mixed ionic−electronic transport in P3MEEET and P3MEEMT through blending with PS and the fabrication of porous films through selective dissolution. Both approaches introduce pronounced phase separation, which strongly influences ionic accessibility and transport pathways. SEC and EIS collectively show that porous films enable greater ion penetration and higher effective volumetric capacitance, whereas blend films restrict ionic ingress as PS content increases.

In OECT devices, the OMIEC:PS blends exhibited markedly enhanced OECT performance. The 11:5 blend films of both polymer series in particular exhibited substantial improvements in μC^* and charge carrier mobility—up to 2−2.5 times relative to pristine films—enabled by reduced swelling. In contrast, porous films exhibited excessive ion and water uptake disrupting electronic transport, consistent with their passive swelling behavior from QCM. Transient response measurements indicated that ionic−electronic coordination can be accurately adjusted through morphological modifications. The incorporation of PS was found to decrease latency from electronic transport in pristine P3MEEET and optimize switching kinetics in the 11:5 blend, whereas introducing porosity slightly enhanced switching in P3MEEMT by improving ionic access.

The ex situ and in situ GIWAXS experiments provided mechanistic insights into these trends, indicating that lattice expansion during hydration and doping is markedly reduced in blend films while being enhanced in porous films. These results, in conjunction with QCM, suggest that swelling primarily impacts amorphous regions, thereby separating the crystallized areas and obstructing the electronic pathways.

Overall, we propose that PS blending is effective in mitigating excessive swelling, thereby preserving electronic transport, while porous architectures facilitate ion injection by providing additional pathways for ions and water, which lead to enhanced swelling that can negatively impact electronic mobility in the present case. However, the selective dissolution approach holds significant potential for application to other polymer systems that could enhance OECT performance.[10,12,49−51] Overall, this work helps to establish morphology manipulation through blending and selective dissolution as a powerful route to engineer mixed transport and transient response in OMIEC-based devices.

EXPERIMENTAL SECTION

Materials

Poly(3-([2-(2-methoxyethoxy)ethoxy]ethyl) thiophene-2,5-diyl) (P3MEEET, M_w = 123 kDa, M_n = 24 kDa, $Đ$ = 5.1) and Poly(3-([2-(2-methoxyethoxy)ethoxy]methyl) thiophene-2,5-diyl) (P3MEEMT, M_w = 70 kDa, M_n = 20 kDa, $Đ$ = 3.4) were purchased from Rieke Metals, Polystyrene (PS, M_w = 183 kDa, M_n = 177.8 kDa, $Đ$ = 1.03) and sodium chloride (NaCl) were purchased from Sigma-Aldrich. Chloroform and cyclohexane were purchased from Merck Millipore.

Solution and Film Preparation

P3MEEET, P3MEEMT, and PS were separately dissolved in chloroform at a concentration of 10 g/L and then heated at 60 °C for 3 h before mixing. After mixing, all blended solutions were heated at 60 °C for another 1 h and then quenched to room temperature; no additional quenching process, heat treatment, or postpreparation processing was applied to the solutions. After preparation, the solutions were stored in a glovebox before film deposition. All films were prepared via spin-coating at 1000 rpm for 1 min. Prior to spin-coating, the substrates were cleaned by ultrasonication in acetone and isopropanol for 10 min each, then dried using a nitrogen gun. To fabricate the porous samples, the films were then dissolved in cyclohexane for 3.5 h to fully dissolve the polystyrene.

Atomic Force Microscopy (AFM)

Images of films were obtained using a JPK Nanowizard 3 in alternating contact (AC) mode in air at a 20 μm × 20 μm size (at 0.5 Hz). Bruker Model NCHV (nominal resonant frequency 340 kHz) cantilevers were used. Images were processed using Gwyddion (version 2.69).

Scanning Transmission X-Ray Microscopy

STXM measurements were performed at the PolLux beamline at the Swiss Light Source (SLS).[67] Samples for STXM measurement were prepared following the same protocols used elsewhere except that a water-soluble layer of sodium polystyrenesulfonate (NaPSS) layer was first deposited on the glass substrate prior to coating of the sample to aid with float-off. Films were delaminated by floating off in deionized water and then transferred to the TEM grids. Images were taken at 4 different energies: 280 eV (pre-edge), 284.75 eV (preferential absorption by PS), 289.4 eV (preferential absorption by P3MEEMT/P3MEEET), and 320 eV (postedge; sensitive to the thickness only). Line profiles were then taken of select regions, where a full carbon K-edge NEXAFS spectrum was acquired at each point along the line profile. Using reference taken spectra of neat samples, and by calibrating to the known X-ray cross sections of the constituent atoms, the chemical composition as a function of position was determined, expressed as plots of P3MEEMT/P3MEEET thickness and PS thickness vs position. STXM data were processed using the IDL widget aXis2000.[68]

Near-Edge X-Ray Absorption Fine Structure Spectroscopy (NEXAFS)

Carbon K-edge NEXAFS spectroscopy measurements were performed at the soft X-ray beamline at the Australian synchrotron. Each sample was also measured at five different polar angles of incidence, namely, 20, 40, 55, 70, and 90°, where an angle of 90° corresponds to normal incidence and an angle of 20° corresponds to glancing incidence. Signals were acquired using pseudo-electron yield (PEY) mode using a hemispherical energy analyzer. Data were analyzed using QANT,[69] with further details of experiment methods and data analysis provided elsewhere.[70]

UV−Vis Spectroscopy

UV−vis spectra were acquired with a PerkinElmer Lambda 950 UV−vis-NIR spectrometer.

CV and Spectroelectrochemistry (SEC)

CV measurements were performed using a VMP-3-based Biologic potentiostat. The three-electrode setup consisted of Ag/AgCl as the reference electrode, a Pt wire as the counter electrode, and polymer thin films on ITO-coated glass substrates as the working electrode, scans were recorded at a scan rate of 50 mV s^{-1}. Three CV cycles were performed on each sample to ensure that there are no obvious irreversible changes under a high potential. Spectroelectrochemistry measurements were performed using an Ocean Optics DH-2000 Deuterium Tungsten Halogen light source combined with a SP-50 Biologic potentiostat. The polymer films on ITO-coated glasses were placed in Hellma Analytics high precision quartz cuvettes. All films were measured under a three-electrode setup with 0.1 M NaCl solution as mentioned above. The spectra were collected under the mode of staircase voltammetry from 0 to 0.9 V with a 0.1 V step for a duration of 2 min.

https://doi.org/10.1021/acsami.6c05714
ACS Appl. Mater. Interfaces 2026, 18, 30250−30268

Electrochemical Impedance Spectroscopy (EIS)

Measurements were performed on polymer-coated gold electrodes (0.0025 cm^2) with a VMP-3 based biologic potentiostat. The impedance spectra were measured in 0.1 M NaCl solution using a Ag/AgCl wire as reference electrode and with a platinum wire as counter electrode. The experiment was conducted at a 0.8 V DC offset for the polymer films and an AC amplitude of 10 mV between 1 Hz and 10^5 Hz. Capacitances are calculated from the following formula obtained by impedance magnitude equation:

$$C = \frac{1}{2\pi f |Z_{img}|} \quad (1)$$

where f is the frequency and $|Z_{img}|$ is the imaginary part of the impedance. The effective volumetric capacitance was calculated by dividing the measured capacitance by its volume, where the film thickness was determined using a Bruker Dektak surface profilometer for the case of pure samples. For blend and porous samples, the UV−vis data was used to determine the effective thickness of the film. Neat samples (whose thickness was measured with the profilometer) were used to calibrate absorbance values measured by UV−vis to thickness values. For the porous samples, the film thickness was estimated by multiplying the thickness of the neat film by the ratio of the UV−vis absorbance of the porous sample to that of the corresponding neat film. For the blend samples, the thickness was first estimated using the same UV−vis absorbance ratio method and was subsequently normalized by the component ratio of the corresponding active polymer. Scanning Transmission X-ray Microscopy (STXM) was used as a complementary technique to assess the local film thickness within a selected region of approximately 20 μm × 20 μm. Although STXM offers high spatial precision, its limited measurement area may not fully capture thickness variations across the entire film.

OECT Characterization

The substrates of the devices were received from the Fraunhofer Institute for Electronic Nano Systems in Chemnitz. The architecture comprises a silicon oxide wafer, a 10 nm chromium adhesion layer, and 100 nm patterned gold electrodes, along with two parylene C layers, each with a thickness of 2 μm. The channel widths ranged from 5 to 15 μm. OECTs were characterized using an Agilent B2902A 2-channel source measure unit in conjunction with a homemade probe station. A PDMS holder was placed onto the substrate, and its cavity was filled with 0.1 M NaCl (aq.) electrolyte. The Ag/AgCl gate electrode was placed in the droplet of the electrolyte. The figure of merit was extracted by plotting the transconductance (g_m) vs $\frac{Wd}{L}|V_G - V_T|$ and fitting the linear regime according to Bernard's model:[65]

$$g_m = \frac{Wd}{L}\mu C^* |V_G - V_T| \quad (2)$$

where g_m is the transconductance, W is the gate width, L is the gate length, d is the film thickness determined by UV−vis spectroscopy for blend and porous samples as discussed earlier and calculated from the profilometer for the pure samples, μ is the mobility, C^* is the effective volumetric capacitance, V_G is the gate voltage, and V_T is the threshold voltage.

Measurement of Transient Response

Transient drain current was measured by applying a V_G pulse of −0.8 V using Agilent B2902A source measure unit at a 0.8 V constant drain voltage. The switch-on time is determined by fitting with the exponential decay function as below:

$$I(t) = I_0 + Ae^{t/\tau} \quad (3)$$

Quartz Crystal Microbalance

QCM measurements were conducted utilizing a Q-sense analyzer (QE401, Biolin Scientific, Gothenburg, Sweden). The frequency and dissipation response are measured on bare Au sensors (QSX 301, Q-Sense AB, Västra Frölunda, Sweden) in both air and a 0.1 M NaCl solution. The polymer-coated Au sensors were then measured under the same conditions as earlier. The absolute frequency values for each polymer-coated sensor were obtained in both air and 0.1 M NaCl solutions once the f signal stabilized (f < 0.5 Hz), confirming that the system reached equilibrium. The absolute differences in frequency for multiple overtones (1st, 3rd, 5th, 7th, 9th, 11th, and 13th) between the bare sensor and the polymer-coated sensors were compared in both air and 0.1 M NaCl solutions. The mass change was calculated using the 7th overtone with the Sauerbrey equation:

$$\Delta m = -\frac{17.7}{n}\Delta f_n \quad (4)$$

where Δm is the mass change, n is the overtone number, and Δf_n is the change of the frequency on the specific overtone number. The mass differences were subsequently converted to volume differences, and the swelling was calculated as follows:

$$\text{Swelling \%} = \frac{V_{swollen} - V_{dry}}{V_{dry}} \times 100\%$$

where $V_{swollen}$ is the volume of the film under the swelling stage, and V_{dry} is the volume of the film under dry stage.

Grazing Incidence Wide-Angle X-ray Scattering

Ex situ GIWAXS measurements were conducted at the SAXS/WAXS beamline of the Australian Synchrotron. Samples for GIWAXS measurements were spin-coated onto bare Si substrates. X-rays with 15 keV energy were applied to the materials at angles between 0.07 and 0.13°. The exposure duration was 1 s. The measurement for each incident angle was recorded at a new location to prevent beam damage. Scattering patterns were acquired using a two-dimensional Dectris Pilatus 2 M detector, featuring a pixel size of 0.172 mm × 0.172 mm, positioned 696 mm downstream from the sample stage. Samples were tested in a vacuum, with the entire beam path enclosed to reduce air scattering. GIWAXS data were analyzed using a modified Nika package in Igor Pro 8; in situ GIWAXS measurements were conducted using the rolling drop setup as described by Flagg et al.[66] In passive swelling measurements, samples were coated on bare Si substrates, 45 μL DI water was dispensed between the glass blade and the substrate, the blade height was 150 μm, the 15 keV X-ray was applied continuously for 30 s during the time when water was vaporized after the blade was moved; In the measurement of active swelling, a silver-coated blade with approximately 200 nm of Ag and a 10 nm Cr adhesion layer was utilized. The potential between the sample and the blade was regulated by an Agilent B2902A two-channel source measure unit. The beam was applied following the same procedure outlined in the passive swelling section after the potential was applied. A photo of the setup can be found in Figure S28.

■ ASSOCIATED CONTENT

Supporting Information

The Supporting Information is available free of charge at https://pubs.acs.org/doi/10.1021/acsami.6c05714.

Morphological, spectroscopic, electrochemical, device, swelling, transient-response, and structural characterization of pure, blended, and porous P3MEEET and P3MEEMT films, including AFM, STXM/NEXAFS, CV, SEC, OECT output, EIS, QCM-D, and ex situ/in situ GIWAXS (PDF)

■ AUTHOR INFORMATION

Corresponding Author

Christopher R. McNeill − *Department of Materials Science and Engineering, Monash University, Monash University, Clayton, Victoria 3800, Australia;* orcid.org/0000-0001-5221-878X; Email: Christopher.McNeill@monash.edu

https://doi.org/10.1021/acsami.6c05714
ACS Appl. Mater. Interfaces 2026, 18, 30250−30268

Authors

Qizhe Tang − *Department of Materials Science and Engineering, Monash University, Monash University, Clayton, Victoria 3800, Australia*

Isabelle Barwick − *School of Chemistry, Monash University, Clayton, Melbourne, VIC 3800, Australia*

Qi Han − *School of Science, STEM College, RMIT University, Melbourne, Victoria 3000, Australia;* orcid.org/0000-0002-6974-0344

Benjamin Watts − *Swiss Light Source, Paul Scherrer Institut, Villigen PSI CH-5232, Switzerland*

Lars Thomsen − *Australian Synchrotron, ANSTO, Clayton, Victoria 3168, Australia*

Julian Hungenberg − *Applied Functional Polymers University of Bayreuth, Bayreuth 95447, Germany*

Matthew Gebert − *Department of Materials Science and Engineering, Monash University, Monash University, Clayton, Victoria 3800, Australia;* orcid.org/0000-0003-1363-9498

Fabian Eller − *Dynamics and Structure Formation − Herzig Group, University of Bayreuth, Bayreuth 95447, Germany*

Eva M. Herzig − *Department of Materials Science and Engineering, Monash University, Monash University, Clayton, Victoria 3800, Australia; Dynamics and Structure Formation − Herzig Group, University of Bayreuth, Bayreuth 95447, Germany;* orcid.org/0000-0002-0151-5562

Mukundan Thelakkat − *Applied Functional Polymers and Bavarian Polymer Institute, University of Bayreuth, Bayreuth 95447, Germany;* orcid.org/0000-0001-8675-1398

Keying Guo − *Drug Delivery, Disposition and Dynamics, Monash Institute of Pharmaceutical Sciences, Monash University, Parkville, Victoria 3052, Australia; Faculty of Biotechnology and Food Engineering, Guangdong Technion-Israel Institute of Technology, Shantou 515063, China; Faculty of Biotechnology and Food Engineering, Technion-Israel Institute of Technology, Haifa 3200003, Israel*

Complete contact information is available at: https://pubs.acs.org/10.1021/acsami.6c05714

Author Contributions

Q.T. - Conceptualization, Investigation, Writing - original draft, Methodology, Formal analysis. I.B. - Writing - review and editing, Investigation. Q.H. - Methodology, Investigation, Writing - review and editing, Formal analysis. B.W. - Investigation, Writing - review and editing. L.T. - Investigation, Writing - review and editing. J.H. - Methodology, Writing - review and editing. M.G. - Investigation, Methodology, Writing - review and editing, Software. F.E. - Methodology, Investigation, Writing - review and editing. E.M.H. - Methodology, Writing - review and editing, Supervision, Funding acquisition. M.T. - Methodology, Writing - review and editing, Supervision. Keying Guo - Methodology, Conceptualization, Writing - review and editing, Supervision. C.R.M. - Conceptualization, Investigation, Methodology, Funding acquisition, Writing - review and editing, Formal analysis, Supervision, Project administration.

Notes

The authors declare no competing financial interest.

■ ACKNOWLEDGMENTS

This work was supported by the DFG International Research Training group (IRTG 2818, Proj. Nr. 464 648 18), Optical Excitations in Organic and Inorganic Semiconductors (OPTEXC) and DAAD/Universities Australia through the Australia-Germany Joint Research Cooperation Scheme (57751700). This work was performed in part at the SAXS/WAXS and Soft X-ray beamlines at the Australian Synchrotron, part of ANSTO. The PolLux end station at the Swiss Light Source was financed by the German Ministerium für Bildung und Forschung (BMBF) through contracts 05K16WED, 05K19WE2 and 05K22WE2. The authors thank Dr. Nigel Kirby and Dr. Pablo Mota-Santiago at the SAXS/WAXS beamline (ANSTO) for assistance with GIWAXS measurements and also thank Prof. Rico Tabor for the use of his AFM facilities. Funding: German Research Council (DFG) International Research Training Group "OPTEXC" (IRTG 2818), DAAD/Universities Australia Australia-Germany Joint Research Cooperation Scheme (57751700).

■ REFERENCES

(1) Nawaz, A.; Liu, Q.; Leong, W. L.; Fairfull-Smith, K. E.; Sonar, P. Organic Electrochemical Transistors for In Vivo Bioelectronics. *Adv. Mater.* **2021**, *33* (49), 2101874.

(2) Stephen, M.; Nawaz, A.; Lee, S. Y.; Sonar, P.; Leong, W. L. Biodegradable Materials for Transient Organic Transistors. *Adv. Funct. Mater.* **2023**, *33* (6), 2208521.

(3) Gkoupidenis, P.; Zhang, Y.; Kleemann, H.; Ling, H.; Santoro, F.; Fabiano, S.; Salleo, A.; van de Burgt, Y. Organic mixed conductors for bioinspired electronics. *Nature Reviews Materials* **2024**, *9* (2), 134−149.

(4) Liu, Y.; Feig, V. R.; Bao, Z. Conjugated Polymer for Implantable Electronics toward Clinical Application. *Adv. Healthcare Mater.* **2021**, *10* (17), 2001916.

(5) Saleh, A.; Koklu, A.; Uguz, I.; Pappa, A.-M.; Inal, S. Bioelectronic interfaces of organic electrochemical transistors. *Nature Reviews Bioengineering* **2024**, *2* (7), 559−574.

(6) Zeglio, E.; Inganäs, O. Active Materials for Organic Electrochemical Transistors. *Adv. Mater.* **2018**, *30* (44), 1800941.

(7) Aftab, S.; Zhou, J.; Cheng, Y.; Zhao, D.; Chen, H.; Huang, W. Functional gate modification for OECT-based sensors. *Materials Today Chemistry* **2025**, *48*, No. 102933.

(8) Paulsen, B. D.; Tybrandt, K.; Stavrinidou, E.; Rivnay, J. Organic mixed ionic−electronic conductors. *Nat. Mater.* **2020**, *19* (1), 13−26.

(9) Inal, S.; Rivnay, J.; Suiu, A.-O.; Malliaras, G. G.; McCulloch, I. Conjugated Polymers in Bioelectronics. *Acc. Chem. Res.* **2018**, *51* (6), 1368−1376.

(10) Liu, C.; Deng, J.; Gao, L.; Cheng, J.; Peng, Y.; Zeng, H.; Huang, W.; Feng, L.-W.; Yu, J. Multilayer Porous Polymer Films for High-Performance Stretchable Organic Electrochemical Transistors. *Advanced Electronic Materials* **2023**, *9* (8), 2300119.

(11) Ko, J.; Wu, X.; Surendran, A.; Muhammad, B. T.; Leong, W. L. Self-Healable Organic Electrochemical Transistor with High Transconductance, Fast Response, and Long-Term Stability. *ACS Appl. Mater. Interfaces* **2020**, *12* (30), 33979−33988.

(12) Chen, J.; Huang, W.; Zheng, D.; Xie, Z.; Zhuang, X.; Zhao, D.; Chen, Y.; Su, N.; Chen, H.; Pankow, R. M.; et al. Highly stretchable organic electrochemical transistors with strain-resistant performance. *Nat. Mater.* **2022**, *21* (5), 564−571.

(13) Chen, S.; Hou, K.; Li, T.; Wu, X.; Wang, Z.; Wei, L.; Leong, W. L. Ultra-Lightweight, Highly Permeable, and Waterproof Fibrous Organic Electrochemical Transistors for On-Skin Bioelectronics. *Advanced Materials Technologies* **2023**, *8* (1), 2200611.

(14) Wang, S.; Wang, Y.; Cai, X.; Wang, B.; Zhao, C.; Pan, G.; Harder, C.; Bulut, Y.; Zhang, B.; Zhang, S.; et al. A high-frequency

artificial nerve based on homogeneously integrated organic electrochemical transistors. *Nature Electronics* **2025**, *8* (3), 254−266.
(15) Laswick, Z.; Wu, X.; Surendran, A.; Zhou, Z.; Ji, X.; Matrone, G. M.; Leong, W. L.; Rivnay, J. Tunable anti-ambipolar vertical bilayer organic electrochemical transistor enable neuromorphic retinal pathway. *Nat. Commun.* **2024**, *15* (1), 6309.
(16) Guo, K.; Wustoni, S.; Koklu, A.; Díaz-Galicia, E.; Moser, M.; Hama, A.; Alqahtani, A. A.; Ahmad, A. N.; Alhamlan, F. S.; Shuaib, M.; et al. Rapid single-molecule detection of COVID-19 and MERS antigens via nanobody-functionalized organic electrochemical transistors. *Nature Biomedical Engineering* **2021**, *5* (7), 666−677.
(17) Zheng, J.; Jiang, X.; Bai, S.; Lai, M.; Yu, J.; Chen, M.; Zhou, R.; Jia, Y.; Yan, H.; Liang, Z.; et al. Clinically Accurate Diagnosis of Alzheimer's Disease via Single-Molecule Bioelectronic Label-Free Profiling of Multiple Blood Extracellular Vesicle Biomarkers. *Adv. Mater.* **2025**, *37* (37), No. 2505262.
(18) Qi, G.; Wang, M.; Wang, S.; Zhang, S.; Teng, X.; Bai, H.; Wang, B.; Zhao, C.; Su, W.; Fan, Q.; et al. High-Performance, Single-Component Ambipolar Organic Electrochemical Transistors with Balanced n/p-Type Properties for Inverter and Biosensor Applications. *Adv. Funct. Mater.* **2025**, *35* (2), 2413112.
(19) Yu, J.; Feng, Q.; Zheng, J.; Liu, H.; Liu, H.; Zhou, R.; Jiang, X.; Yan, H.; Liang, Z.; Chen, M.; et al. Small Molecule-Driven Organic Electrochemical Transistors for Rapid, Ultrasensitive and Amplification-Free Detection of RNA Biomarkers. *Adv. Mater.* **2026**, *38* (9), No. e15338.
(20) Jiang, Z.; Ye, D.; Xiang, L.; He, Z.; Dai, X.; Yang, J.; Xiong, Q.; Ma, Y.; Zhi, D.; Zou, Y.; et al. A drug-mediated organic electrochemical transistor for robustly reusable biosensors. *Nat. Mater.* **2024**, *23* (11), 1547−1555.
(21) Zhang, B.; Xiang, L.; Yan, C.; Jiang, Z.; Zhao, H.; Li, C.; Zhang, F. Morphology-Controlled Ion Transport in Mixed-Orientation Polymers. *ACS Appl. Mater. Interfaces* **2024**, *16* (25), 32456−32465.
(22) Rivnay, J.; Inal, S.; Salleo, A.; Owens, R. M.; Berggren, M.; Malliaras, G. G. Organic electrochemical transistors. *Nature Reviews Materials* **2018**, *3* (2), 17086.
(23) Ohayon, D.; Druet, V.; Inal, S. A guide for the characterization of organic electrochemical transistors and channel materials. *Chem. Soc. Rev.* **2023**, *52* (3), 1001−1023.
(24) Hungenberg, J.; Hochgesang, A.; Meichsner, F.; Thelakkat, M. Self-Doped Mixed Ionic-Electronic Conductors to Tune the Threshold Voltage and the Mode of Operation in Organic Electrochemical Transistors. *Adv. Funct. Mater.* **2024**, *34* (44), 2407067.
(25) Lin, P.; Yan, F.; Chan, H. L. W. Ion-Sensitive Properties of Organic Electrochemical Transistors. *ACS Appl. Mater. Interfaces* **2010**, *2* (6), 1637−1641.
(26) Khodagholy, D.; Rivnay, J.; Sessolo, M.; Gurfinkel, M.; Leleux, P.; Jimison, L. H.; Stavrinidou, E.; Herve, T.; Sanaur, S.; Owens, R. M.; et al. High transconductance organic electrochemical transistors. *Nat. Commun.* **2013**, *4* (1), 2133.
(27) Giridharagopal, R.; Flagg, L. Q.; Harrison, J. S.; Ziffer, M. E.; Onorato, J.; Luscombe, C. K.; Ginger, D. S. Electrochemical strain microscopy probes morphology-induced variations in ion uptake and performance in organic electrochemical transistors. *Nat. Mater.* **2017**, *16* (7), 737−742.
(28) Kim, S.-M.; Kim, C.-H.; Kim, Y.; Kim, N.; Lee, W.-J.; Lee, E.-H.; Kim, D.; Park, S.; Lee, K.; Rivnay, J.; et al. Influence of PEDOT:PSS crystallinity and composition on electrochemical transistor performance and long-term stability. *Nat. Commun.* **2018**, *9* (1), 3858.
(29) Savva, A.; Hallani, R.; Cendra, C.; Surgailis, J.; Hidalgo, T. C.; Wustoni, S.; Sheelamanthula, R.; Chen, X.; Kirkus, M.; Giovannitti, A.; et al. Balancing Ionic and Electronic Conduction for High-Performance Organic Electrochemical Transistors. *Adv. Funct. Mater.* **2020**, *30* (11), 1907657.
(30) Quill, T. J.; LeCroy, G.; Halat, D. M.; Sheelamanthula, R.; Marks, A.; Grundy, L. S.; McCulloch, I.; Reimer, J. A.; Balsara, N. P.; Giovannitti, A.; et al. An ordered, self-assembled nanocomposite with efficient electronic and ionic transport. *Nat. Mater.* **2023**, *22* (3), 362−368.
(31) Schmode, P.; Savva, A.; Kahl, R.; Ohayon, D.; Meichsner, F.; Dolynchuk, O.; Thurn-Albrecht, T.; Inal, S.; Thelakkat, M. The Key Role of Side Chain Linkage in Structure Formation and Mixed Conduction of Ethylene Glycol Substituted Polythiophenes. *ACS Appl. Mater. Interfaces* **2020**, *12* (11), 13029−13039.
(32) Guo, J.; Flagg, L. Q.; Tran, D. K.; Chen, S. E.; Li, R.; Kolhe, N. B.; Giridharagopal, R.; Jenekhe, S. A.; Richter, L. J.; Ginger, D. S. Hydration of a Side-Chain-Free n-Type Semiconducting Ladder Polymer Driven by Electrochemical Doping. *J. Am. Chem. Soc.* **2023**, *145* (3), 1866−1876.
(33) Rinehart, J. M.; Xu, Z.; Wang, Z.; Österholm, A. M.; Flagg, L. Q.; Richter, L. J.; Snyder, C. R.; Diao, Y.; Reynolds, J. R. Impact of Side-Chain Polarity and Symmetry on the Structure and Properties of Acyclic Dioxythiophene Polymers. *Chem. Mater.* **2025**, *37* (13), 4593−4606.
(34) Chen, S. E.; Flagg, L. Q.; Onorato, J. W.; Richter, L. J.; Guo, J.; Luscombe, C. K.; Ginger, D. S. Impact of varying side chain structure on organic electrochemical transistor performance: a series of oligoethylene glycol-substituted polythiophenes. *Journal of Materials Chemistry A* **2022**, *10* (19), 10738−10749.
(35) Surgailis, J.; Flagg, L. Q.; Richter, L. J.; Druet, V.; Griggs, S.; Wu, X.; Moro, S.; Ohayon, D.; Kousseff, C. J.; Marks, A.; et al. The Role of Side Chains and Hydration on Mixed Charge Transport in n-Type Polymer Films. *Adv. Mater.* **2024**, *36* (51), 2313121.
(36) Moser, M.; Hidalgo, T. C.; Surgailis, J.; Gladisch, J.; Ghosh, S.; Sheelamanthula, R.; Thiburce, Q.; Giovannitti, A.; Salleo, A.; Gasparini, N.; et al. Side Chain Redistribution as a Strategy to Boost Organic Electrochemical Transistor Performance and Stability. *Adv. Mater.* **2020**, *32* (37), 2002748.
(37) Cho, Y.; Gao, L.; Yao, Y.; Kim, J.; Zhang, D.; Forti, G.; Duplessis, I.; Wang, Y.; Pankow, R. M.; Ji, X.; et al. Small-Molecule Mixed Ionic-Electronic Conductors for Efficient N-Type Electrochemical Transistors: Structure-Function Correlations. *Angew. Chem., Int. Ed.* **2025**, *64* (2), No. e202414180.
(38) Lan, L.; Wang, Y.; Zhu, X.; McCulloch, I.; Yue, W. Ultrathin-Film Small Molecule Mixed Conductors Exhibiting Ion-Tunable Ambipolarity for High-Performance Organic Electrochemical Transistors and Multivalued Logic Inverters. *Adv. Mater.* **2025**, *37* (35), No. 2501041.
(39) Quill, T. J.; LeCroy, G.; Marks, A.; Hesse, S. A.; Thiburce, Q.; McCulloch, I.; Tassone, C. J.; Takacs, C. J.; Giovannitti, A.; Salleo, A. Charge Carrier Induced Structural Ordering And Disordering in Organic Mixed Ionic Electronic Conductors. *Adv. Mater.* **2024**, *36* (15), 2310157.
(40) Erhardt, A.; Hochgesang, A.; McNeill, C. R.; Thelakkat, M. A Competitive n-Type OECT Material via Copolymerization of Electron Deficient Building Blocks. *Advanced Electronic Materials* **2023**, *9* (7), 2300026.
(41) Gunturkun, D.; Meli, D.; Thorley, K. J.; Kuhn, M.; Herzig, E. M.; Rivnay, J.; Nielsen, C. B. Impact of donor modification on azaisoindigo-based polymers for n- and p-type organic electrochemical transistors. *Journal of Materials Chemistry C* **2025**, *13* (44), 22244−22252.
(42) Kim, J. H.; Halaksa, R.; Jo, I.-Y.; Ahn, H.; Gilhooly-Finn, P. A.; Lee, I.; Park, S.; Nielsen, C. B.; Yoon, M.-H. Peculiar transient behaviors of organic electrochemical transistors governed by ion injection directionality. *Nat. Commun.* **2023**, *14* (1), 7577.
(43) Flagg, L. Q.; Bischak, C. G.; Onorato, J. W.; Rashid, R. B.; Luscombe, C. K.; Ginger, D. S. Polymer Crystallinity Controls Water Uptake in Glycol Side-Chain Polymer Organic Electrochemical Transistors. *J. Am. Chem. Soc.* **2019**, *141* (10), 4345−4354.
(44) Hidalgo Castillo, T. C.; Shan, W.; Ma, G.; Zhao, H.; Wang, Y.; Druet, V.; Saleh, A.; Gu, X.; Inal, S. Thermal Annealing for High Performance and Memory Behavior in n-Type Organic Electrochemical Transistors. *Adv. Mater.* **2025**, *37* (5), 2411214.
(45) Zhu, X.; Chen, J.; Liu, R.; Chen, C.; Tan, J.; Ran, C.; Wang, Y.; Wang, R.; Li, Z.; Yue, W. Modulating crystallinity and mixed ionic−

https://doi.org/10.1021/acsami.6c05714
ACS Appl. Mater. Interfaces 2026, 18, 30250−30268

electronic conduction properties via terminal side chain engineering of n-type small molecules. *Journal of Materials Chemistry C* **2025**, *13* (4), 1784−1792.
(46) Huang, W.; Chen, J.; Yao, Y.; Zheng, D.; Ji, X.; Feng, L.-W.; Moore, D.; Glavin, N. R.; Xie, M.; Chen, Y.; et al. Vertical organic electrochemical transistors for complementary circuits. *Nature* **2023**, *613* (7944), 496−502.
(47) Wang, B.; Kong, Y.; Zhang, S.; Wu, Z.; Wang, S.; Ren, J.; Woo, H. Y.; Li, Y.; Ma, W. Face-on Orientation Matches Vertical Organic Electrochemical Transistors for High Transconductance and Superior Non-Volatility. *Adv. Funct. Mater.* **2024**, *34* (14), 2312822.
(48) Yan, C.; Xiang, L.; Xiao, Y.; Zhang, X.; Jiang, Z.; Zhang, B.; Li, C.; Di, S.; Zhang, F. Lateral intercalation-assisted ionic transport towards high-performance organic electrochemical transistor. *Nat. Commun.* **2024**, *15* (1), 10118.
(49) Lan, L.; Chen, J.; Wang, Y.; Li, P.; Yu, Y.; Zhu, G.; Li, Z.; Lei, T.; Yue, W.; McCulloch, I. Facilely Accessible Porous Conjugated Polymers toward High-Performance and Flexible Organic Electrochemical Transistors. *Chem. Mater.* **2022**, *34* (4), 1666−1676.
(50) Yang, H. S.; Kim, W.; Yoo, H.; Lee, E. K. Organic Electrochemical Transistors with Microporous Structures via Phase-Separation for Enhancing Long-Term Plasticity in Artificial Synapses. *Advanced Materials Technologies* **2024**, *9* (24), 2400478.
(51) Huang, L.; Wang, Z.; Chen, J.; Wang, B.; Chen, Y.; Huang, W.; Chi, L.; Marks, T. J.; Facchetti, A. Porous Semiconducting Polymers Enable High-Performance Electrochemical Transistors. *Adv. Mater.* **2021**, *33* (14), 2007041.
(52) Bischak, C. G.; Flagg, L. Q.; Yan, K.; Rehman, T.; Davies, D. W.; Quezada, R. J.; Onorato, J. W.; Luscombe, C. K.; Diao, Y.; Li, C.-Z.; et al. A Reversible Structural Phase Transition by Electrochemically-Driven Ion Injection into a Conjugated Polymer. *J. Am. Chem. Soc.* **2020**, *142* (16), 7434−7442.
(53) Li, T.; Qu, Z.; Si, J.; Lee, Y.; Bandari, V. K.; Schmidt, O. G. Monolithically integrated solid-state vertical organic electrochemical transistors switching between neuromorphic and logic functions. *Sci. Adv.* **2025**, *11* (11), No. eadt5186.
(54) Kim, J.; Pankow, R. M.; Cho, Y.; Duplessis, I. D.; Qin, F.; Meli, D.; Daso, R.; Zheng, D.; Huang, W.; Rivnay, J.; et al. Monolithically integrated high-density vertical organic electrochemical transistor arrays and complementary circuits. *Nature Electronics* **2024**, *7* (3), 234−243.
(55) Rashid, R. B.; Du, W.; Griggs, S.; Maria, I. P.; McCulloch, I.; Rivnay, J. Ambipolar inverters based on cofacial vertical organic electrochemical transistor pairs for biosignal amplification. *Sci. Adv.* **2021**, *7* (37), No. eabh1055.
(56) Kuo, C.-T.; Lin, Y.-S.; Liu, T.-K.; Liu, H.-C.; Hung, W.-C.; Jiang, I. M.; Tsai, M.-S.; Hsu, C.-C.; Wu, C.-Y. Dynamics of single-layer polymer breath figures. *Opt. Express* **2010**, *18* (17), 18464−18470.
(57) Tang, L.; Thomsen, L.; McNeill, C. R. Chain Alignment and Charge Transport Anisotropy in Blade-Coated P(NDI2OD-T2)/PS Blend Films. *ACS Applied Polymer Materials* **2022**, *4* (8), 5501−5514.
(58) Tang, L.; Watts, B.; Thomsen, L.; McNeill, C. R. Morphology and Charge Transport Properties of P(NDI2OD-T2)/Polystyrene Blends. *Macromolecules* **2021**, *54* (23), 11134−11146.
(59) Strakosas, X.; Sessolo, M.; Hama, A.; Rivnay, J.; Stavrinidou, E.; Malliaras, G. G.; Owens, R. M. A facile biofunctionalisation route for solution processable conducting polymer devices. *J. Mater. Chem. B* **2014**, *2* (17), 2537−2545.
(60) Zeglio, E.; Wang, Y.; Jain, S.; Lin, Y.; Avila Ramirez, A. E.; Feng, K.; Guo, X.; Ose, H.; Mozolevskis, G.; Mawad, D.; et al. Mixing Insulating Commodity Polymers with Semiconducting n-type Polymers Enables High-Performance Electrochemical Transistors. *Adv. Mater.* **2024**, *36* (23), 2302624.
(61) Nguyen, D. C. T.; Vu Thi, Q.; Nguyen, Q. H.; Ko, J.; Lee, H.; Boudouris, B.; Jeon, S.-Y.; Joo, Y. Engineering flexible dopamine biosensors: blended EGylated conjugated and radical polymers in organic electrochemical transistors. *npj Flexible Electronics* **2025**, *9* (1), 35.
(62) Wang, Z.; Qiu, W.; Zhang, Q. Constructing phase separation in polymer gels: Strategies, functions and applications. *Prog. Polym. Sci.* **2024**, *154*, No. 101847.
(63) Friedel, B.; Ehrler, B.; Hüttner, S.; Greenham, N. C. Enhanced Nanoscale Imaging of Polymer Blends by Temperature-Controlled Selective Dissolution. *Small* **2012**, *8* (2), 237−240.
(64) Chung, S. H.; Song, J. H.; Lee, W. W.; Yoo, H.; Lim, H.-R.; Lee, E. K. Tailored phase separation in P3HT:PS blends for enhanced synaptic performance in organic electrochemical transistors. *Synth. Met.* **2025**, *314*, No. 117919.
(65) Bernards, D. A.; Malliaras, G. G. Steady-State and Transient Behavior of Organic Electrochemical Transistors. *Adv. Funct. Mater.* **2007**, *17* (17), 3538−3544.
(66) Flagg, L. Q.; Asselta, L. E.; D'Antona, N.; Nicolini, T.; Stingelin, N.; Onorato, J. W.; Luscombe, C. K.; Li, R.; Richter, L. J. In Situ Studies of the Swelling by an Electrolyte in Electrochemical Doping of Ethylene Glycol-Substituted Polythiophene. *ACS Appl. Mater. Interfaces* **2022**, *14* (25), 29052−29060.
(67) Raabe, J.; Tzvetkov, G.; Flechsig, U.; Böge, M.; Jaggi, A.; Sarafimov, B.; Vernooij, M. G. C.; Huthwelker, T.; Ade, H.; Kilcoyne, D.; et al. PolLux: A new facility for soft x-ray spectromicroscopy at the Swiss Light Source. *Rev. Sci. Instrum.* **2008**, *79* (11), 113704.
(68) Hitchcock, A. P. Analysis of X-ray images and spectra (aXis2000): A toolkit for the analysis of X-ray spectromicroscopy data. *J. Electron Spectrosc. Relat. Phenom.* **2023**, *266*, No. 147360.
(69) Dudenas, P. J.; Flagg, L. Q.; Goetz, K.; Shapturenka, P.; Fagan, J. A.; Gann, E.; DeLongchamp, D. M. How to RSoXS. *J. Chem. Phys.* **2025**, *163* (6), No. 061501.
(70) Nahid, M. M.; Gann, E.; Thomsen, L.; McNeill, C. R. NEXAFS spectroscopy of conjugated polymers. *Eur. Polym. J.* **2016**, *81*, 532−554.

https://doi.org/10.1021/acsami.6c05714
ACS Appl. Mater. Interfaces 2026, 18, 30250−30268